Microwave penetration in polar snow and ice: Implications for GPR and SAR

Karsten Müller

Department of Geosciences

Faculty of Mathematics and Natural Sciences
University of Oslo

A thesis submitted for the degree of *Philosophiae Doctor*

(PhD)

Oslo, Norway 2011

Series of dissertations submitted to the
Faculty of Mathematics and Natural Sciences, University of Oslo
No. 1090

ISSN 1501-7710

Cover: Inger Sandved Anfinsen.
Printed in Norway: AIT Oslo AS.

Produced in co-operation with Unipub.
The thesis is produced by Unipub merely in connection with the
thesis defence. Kindly direct all inquiries regarding the thesis to the copyright
holder or the unit which grants the doctorate.

Abstract

The state of the continental ice masses has a direct impact on the global sea level. Changes in the polar regions will not only impact the people living in the Arctic, but also people living along coastlines around the world.

Monitoring the current and future state of the global ice masses is therefore of greatest interest. Microwave remote sensing of the cryosphere from ground, air or space is an active and fast developing field of research.

In this thesis we investigate the interaction of microwaves with snow and ice by means of ground penetrating radar (GPR) and relate the findings to observations from space-borne radars (SAR or InSAR).

We applied GPR to extend the 200 year mean surface mass balance (SMB) measurement from firn cores in a previously unmapped part of East Antarctica. Our findings show up to 50% lower values than estimated from modelling or remote sensing. However, our evaluated time period is much longer and our spatial resolution much finer. We relate our SMB values to radar backscatter from space-borne radar and use this correlation to further extend the SMB estimate over a 76000 km^2 large area on the East Antarctic plateau.

We investigate the position of the GPR phase center (z_ϕ) in snow, firn and ice in the interior and exterior of the East Antarctic Plateau and a glacier on Svalbard. Values of z_ϕ exceed 40 m in the dry firn of the East Antarctic Plateau at frequencies of 1.75 GHz. Thus, we have to expect a potential bias when measuring topography by means of InSAR in these areas. In coastal Antarctica and on an Arctic glacier z_ϕ often exceeds 5 m even at C-band. Consequently, deriving mass-balance estimates through monitoring elevation changes with radar are difficult to interpret.

However, we find that z_ϕ aligns with the previous summer surface in the ablation zone of the glacier for S- and C-band frequencies. Thus, in this part of the glacier elevation changes can be monitored with InSAR. We attribute the difference in z_ϕ from the ablation zone to the firn zone of the glacier to a change in scattering mechanisms, which results in stronger radar backscatter from the firn zone. We use this difference to map the extent of the firn area by a simple threshold classification.

Acknowledgments

The front page of this dissertation shows only one name, but many persons contributed to it through their inspiration, discussion, curiosity and distraction.

First of all I would like to thank my supervisors Svein-Erik Hamran and Jon-Ove Hagen for making this PhD possible. You both guided me through technical and practical advice. Svein-Erik and Mats-Jørgen Øyan built the radars essential for this dissertation. Anna joined my lonely Antarctic research group at the Department of Geosciences at the right time. She was of great help in many aspects regarding this thesis. Thanks for being kind of my third supervisor, always good for interesting and critical discussions.

Crossing the Antarctic continent is a lifetime experience. It is a unique place and I will long remember the impressions I gained on this trip. Being *forced* to live close together with 11 other people, initially *strangers* truly forms the character. I want to thank the traverse team 2007/2008 - Mary Albert, Jan-Gunnar Winther, Lou Albershardt, Helgard Anschütz, Kjetil Bakkland, John Guldahl, Einar Johanson, Glen Liston, Atsuhiro Muto, Stian Solbø, and Stein Trondstad - for being such a great team in the field.

My time on Svalbard prior to the trip to Antarctica gave me a warm start to the cold environment. I would like to thank the students in the UNIS glaciology course, especially Susanne Ingvander for fun discussions and sharing the trouble one encounters during a PhD and an Antarctic traverse. Many thanks go to Jack Kohler for the opportunity to get properly acclimatised in Ny-Ålesund and providing additional funding towards the end of my PhD.

A lot of my work is based on the PhD thesis of Kirsty Langley. Kirsty was always available for discussion and questions. It is a bit sad that you moved to Tromsø, because I miss the outdoor activities with you and Elvar.

I am thankful for my colleagues at the department. The doors of Thorben Dunse, Chris Nuth, Thomas Schuler, Andy Kääb and Bernd Etzelmüller were always open to me. Thanks to the entire *lunsjrom* group. I very much enjoyed the extended lunch breaks and corridor chats.

I also want to thank Rune Engeset for the patience he had with me as my new boss at NVE. He provided me the freedom and support to finish this thesis beside the new job. I originally promised him to finish in September 2010.

The main funding for this PhD come from the Norwegian Research Council and NARE. Additional funding has been provided through the GLACIODYN IPY project and the Arktisstipend by the Svalbard Science Forum.

Thanks to my family for their constant support. My daughters Frida and Matilda often helped me to forget about work for a little while and showed me how to enjoy life at its best. Last, but not least, my by far biggest gratitude goes to my wife Elisabeth. Thank you for your love and encouragement.

Contents

Chapter 1

Scientific Background

1.1 Introduction

The International Polar Year (IPY) was an internationally coordinated science program including physical, biological, and social research aiming to increase our understanding of the polar regions and their role for the global climate. IPY occurred at a time when the shrinking of glaciers (Kohler et al., 2007) and disintegration of large ice shelves (Scambos et al., 2009; Hulbe et al., 2008) has been witnessed globally by the general public. Snow reflects most incoming solar radiation. As snow extent diminishes, more radiation is absorbed at the Earth surface and the atmosphere will heat up. This leads to a positive feedback loop in which snow and ice will melt faster (Rees, 2006). Natural systems within the polar regions are therefore sensitive to changes in the global climate with response times ranging from several years for small glaciers to several centuries for the ice sheets of Antarctica and Greenland (Alley et al., 2005). Ultimately, the state of the continental ice masses has a direct impact on global sea level. Therefore, changes in the polar regions will have an impact for people living there, as well as for people living along the coastlines around the world.

In order to fully understand the static and dynamic processes of glaciers and ice sheets we need to be able to monitor the polar regions continuously, both in space and time. This task is challenging as the polar regions are vast, hard to access, and without daylight for several months each year. Also, continuous monitoring from ground or air is costly, time consuming and nearly impossible.

Active microwave remote sensing instruments operate independent of daylight or

cloud cover and they can be operated on-board satellites to provide large spatial and high temporal coverage. Today, several microwave instruments are available and future space missions are specifically dedicated to measuring snow and ice. In contrast to sensors operating in the visible part of the electromagnetic (EM) spectrum, microwaves penetrate substantially into the snowpack and therefore the signal is a result of geometric and bulk-dielectric properties of both the surface and volume that reflect the EM waves (Ulaby et al., 1986). Knowledge of the depth of the snow volume contributing to emission and backscattering is essential for the interpretation of microwave signatures (Rott et al., 1993). Thus, the advantage of continuous monitoring is opposed by a more complicated and often ambiguous interpretation of the observed return signal compared to an optical image.

In this dissertation, we investigate microwave penetration into snow and ice for the retrieval of glaciological parameters by means of radar. We apply ground penetrating radar (GPR) to study the surface mass balance along a profile on the East Antarctic Plateau and use an empirical relation between GPR derived SMB and SAR backscatter to extend our SMB estimate over a wider area. We calculate the phase center, which indicates the distance to the dominating scattering source, along GPR traces recorded in different polar environments and relate it to SAR backscatter and the snow stratigraphy evident from the GPR profiles.

1.2 Radar

Radar(RAdio Detection And Ranging) is a technique to retrieve information about remote targets using reflected EM waves in the microwave spectrum. Radar is an active measuring device. A transmitter emits an EM wave via an antenna in the direction of the target. The wave will be partially absorbed and partially reflected at the target. The portion of the energy reflected back to the receiving antenna, i.e. backscatter, is used to characterize the target depending on amplitude, phase, polarization, and travel-time of the return signal. The amplitude of the returned energy can be used to characterize the target based upon the target's or medium's dielectric properties and physical size. Changes in the phase and polarization of a microwave after interacting with a target depends on the dielectric contrast and the scattering mechanisms involved.

We can use the travel-time to and from the target and/or the phase to determine the distance between the radar and the target.

Ground based geophysical radar applications commonly use the frequency range from 1 MHz to 3 GHz, while active air- or space-borne radar instruments for geoscience applications operate at frequencies up to 18 GHz. The lower frequencies in this range are used in radar sounding applications when the goal is to penetrate as deep as possible and map internal structures of a medium. The higher frequencies in this range are used for accurate distance measurements to map elevation and monitor elevation changes, e.g. radar altimetry. In the case of radar remote sensing of snow and ice, the advantages of using active microwave instruments lie in their low energy losses in snow and ice in the sub GHz spectrum and their independence of light or cloud conditions for large scale monitoring from air or space.

1.2.1 Radar in glaciology: A brief overview

GPR has been applied in glaciological studies for the past several decades (Bogorodsky et al., 1985). Snow and ice are radar friendly materials, meaning microwaves experience very low attenuation while traveling through them. This allows us to investigate the internal structure of snowpacks, glaciers, and ice-sheets. GPR in the frequency range between 50-1000 MHz is readily used in mass-balance studies on glaciers and ice-sheets (Eisen and Others, 2008; Arcone et al., 2005; Fujita et al., 1999; Richardson et al., 1997). At these frequencies it is possible to map the snow or ice stratigraphy to ≈200 m depth. The reflections in the GPR record stem from contrasts in the dielectric permittivity between isochronal surfaces (Eisen and Others, 2008). Calibration by ice core records or snow pits is necessary to date the isochrones.

Radio frequencies lower than 50 MHz can penetrate entire glaciers, ice-shelves or ice-sheets and therefore used to study bed conditions and/or drainage systems (Matsuoka et al., 2010; MacGregor et al., 2007; Murray et al., 2000; Jenkins and Doake, 1991). Although GPR surveys can be conducted from snowmobiles or tracked vehicles the potential coverage remains relatively small compared to the vast spatial extent of larger ice masses.

Microwave observations from space-borne platforms have become an imporatant tool for continuous monitoring of the polar regions. Their ability to provide measure-

ments unaffected by cloud cover or in the absence of daylight make them applicable year-round with short repeat cycles. Synthetic aperture radars (SAR) provide a two-dimensional image of backscatter intensity. Temporal changes in backscatter of snow, firn or ice can be related to melt events or snow metamorphism (Bingham and Drinkwater, 2000). SAR backscatter scenes are used to study glaciers by detecting the firn edge for mass-balance monitoring (Engeset et al., 2002; König et al., 2001), classifying different glacier zones (Langley et al., 2008), or relating backscatter values directly to accumulation rates (Rotschky et al., 2006). Ice dynamics or glacier mass-balance can be studied by interferometric SAR (InSAR) that measures ground movement and/or topography (Rignot and Thomas, 2002) by comparing two or more SAR scenes with a spatial or temporal offset to each other.

The first space-borne microwave instrument used for observing the polar regions was the radar altimeter on-board GEOS-3 in 1978. Originally designed for measuring sea surface height and the geoid over the oceans, it was also applied to measure the elevation of the large ice sheets, Antarctica and Greenland (Brooks et al., 1978). Large scale monitoring of the polar regions using space-borne radar systems started with the European Remote Sensing satellite (ERS-1) in 1991, followed by ERS-2 and the Canadian RadarSat-1 in 1995. The tandem mission of ERS-1 and -2 in 1996/97 provided a new set of InSAR data over glaciers and ice-sheets below 80°S, allowing ice velocity and ice thickness changes to be measured over large regions in Antarctica and the Arctic. In 1998 the SAR instrument on-board RadarSat-1 was turned by 180° to look towards the poles and overcome the limitation of 80°S and map Antarctica as a whole (Jezek and Team, 2002). The launch of the Japanese satellite Alos with its Phased Array type L-band Synthetic Aperture Radar (PALSAR) in early 2006 lead to an increase of L-band data in cryospheric sciences (Rignot, 2008). L-bands (1.2 GHz) longer wavelength (compared to the common C-band) allows deeper penetration in snow or ice. The signal is less sensitive to near-surface changes of the snowpack and yields higher coherence between measurements with a longer temporal offset. This is an advantage for glacier flow velocity measurements with interferometric SAR, since image coherence is less influenced by the quickly changing surface conditions (Rignot et al., 2001).

Valuable data about the cryosphere have been so far provided by the microwave

SAR and altimeters on current missions, like EnviSat, Alos, and RadarSat-2, but before the launch of CryoSat-2 in April 2010 there was no space-borne radar instrument solely dedicated and specifically designed to monitor the cryosphere. CryoSat-2 carries the SIRAL-2 instrument, a Ku-band frequency radar altimeter that has a SAR and interferometric mode. Another planned mission is the CoreH2O mission (Rott et al., 2008). On-board will be an X- and Ku-band frequency SAR. The difference in frequency between the two signals will lead to a difference in penetration depth in snow. While the X-band is expected to penetrate seasonal snowcover completely, the main backscatter (or phase center) from the Ku-band radar is expected to return from the air-snow boundary. Thus, using these two radars should allow an estimate of the snow water equivalent (SWE) of a dry seasonal snow pack.
Although essential for the CoreH2O mission, penetration of microwaves into snow and ice can complicate signal interpretation and bias measurements of elevation from radar altimeters or InSAR operated from air or space.

1.2.2 The radar equation

The power received at the radar from energy backscattered at a volume distributed incoherent target is given by the radar equation (Ulaby et al., 1981)

$$P_r = P_t \frac{G^2 \lambda^2}{(4\pi)^3 z^4} \sigma e^{-2\tau(z)} \quad [W], \tag{1.2.1}$$

where

- P_r: received power [W],
- P_t: transmitted power [W],
- G: antenna gain,
- λ: wavelength [m],
- z: range to target [m],
- σ: scattering cross section [m^2]
- $\tau(z) = \int_0^z \kappa_e(z')dz'$: extinction term [Np m]

G is a measure of how much more power density the antenna is able to transmit in the preferred direction than can the equivalent isotropic source (Richards, 2008). σ describes the area of the target with regard to an isotropic scatterer that would return the same power equally distributed in all directions. Meaning, a large σ characterizes a strong reflector and a small σ a weak reflector. In the case of a mono-static radar, where transmitter and receiver antenna are located at the same position, σ depends on the portion of the power scattered back towards the sensor and is termed backscatter cross section (σ^0). The extinction term τ describes how the wave looses energy while traveling through the volume. By multiplying σ^0 by the incident power density S_i the total power radiated by an equivalent isotropic radiator S_s can be solved given a known distance, R, from the scatterer,

$$S_s(\pi) = \frac{S_i \sigma^0}{4\pi R^2} \Leftrightarrow \sigma^0 = 4\pi R^2 (S_s(\pi)/S_i) \quad , \tag{1.2.2}$$

where π indicates the direction back to the sensor and σ^0 is in units of m^2 (Ulaby et al., 1982).

The radar system constants can be combined into the constant C_i

$$C_i = P_t (4\pi)^{-3} G^2 \lambda^2 \tag{1.2.3}$$

σ^0 is equal to the backscattering cross-section per unit volume, σ_v^0, integrated over the contributing volume (Ulaby et al., 1981). For a narrow-beam antenna with half-power beam width θ, the contributing volume at a range z is

$$V(z, \theta) = \pi z^2 \sin^2(\theta) \Delta z, \tag{1.2.4}$$

where Δz is the pulse width. If σ_v is approximately uniform over V, then

$$\sigma^0 = \sigma_v^0 V \quad [m^2]. \tag{1.2.5}$$

Combining equations 1.2.1, 1.2.3, and 1.2.5 we yield the following radar equation for volume distributed incoherent targets

$$P_r = C_i V(z) \sigma_v^0(z) e^{-2\tau(z)} \quad [W]. \tag{1.2.6}$$

1.2.3 Frequency-modulated continuous-wave radar

Frequency modulated continuous wave (FMCW) radars transmit a chirp. A chirp is a long pulse with linear frequency modulation. It has the advantage of achieving high radiometric resolution without the high power requirements of a short pulse (Daniels, 2004). The portion of the signal returning to the receiver after reflection at a target is mixed with a copy of the transmitted signal in order to determine the range to the target. The difference between the highest and lowest transmitted frequency is the bandwidth B of the radar. The sweep time T is the time it takes to sweep over the bandwidth. The rate of change α is defined by BT^{-1}. The transmitted waveform travels to the target at range R and back in time

$$\tau_R = \frac{2R}{c_{med}} \tag{1.2.7}$$

where c_{med} is the velocity of light in the medium (Ulaby et al., 1981). If the start frequency is denoted f_0, the transmitted frequency f_t is then

$$f_t(t) = f_0 + \alpha t \tag{1.2.8}$$

and the received frequency f_r (in case of an ideal point target) is

$$f_r(t) = f_0 + \alpha(t - \tau_R). \tag{1.2.9}$$

Mixing the transmitted and received signals results in a sum (f_t+f_r) and a difference frequency ($f_t - f_r$). Low pass filtering removes the sum and leaves the difference frequency as the so called beat frequency

$$f_b = f_t - f_r = \alpha\tau_R = \frac{B}{T} \cdot \frac{2R}{c_{med}}, \tag{1.2.10}$$

which can be re-arranged to the following expression for the target range

$$R = f_b \frac{T c_{med}}{2B}. \tag{1.2.11}$$

When multiple targets exist, the result will be a superposition of many beat frequencies. An inverse Fourier Transform yields a trace of amplitudes versus distance to the targets with regard to their f_b. In the frequency domain two targets beat frequency can be as close together as T^{-1} and still be resolved (Ulaby et al., 1981). From equation (1.2.10) we get the difference in delay time τ_R between two targets as

$$\Delta\tau_R = \frac{T}{B}\Delta f_b. \tag{1.2.12}$$

Inserting $f_b = T^{-1}$ gives the minimum $\Delta\tau_R = B^{-1}$, which leads to the range resolution using (1.2.7)

$$\Delta R = \frac{c_{med}}{2}\Delta\tau_R = \frac{c_{med}}{2B}. \tag{1.2.13}$$

The ambiguous range depends on the frequency sampling and is given by

$$R_{amb} = \frac{c}{2\Delta f} \tag{1.2.14}$$

FMCW radars allow short pulses while maintaining high mean power. This makes FMCW radars more suitable for high-resolution applications than impulse radars, which would require more power and more complex, thus more expensive, hardware. We recommend reading Marshall and Koh (2008); Daniels (2004); Ulaby et al. (1981) for further details about FMCW radar.

We used two different FMCW radars within the frame of this thesis (Fig. 1.1). The first is a C-band system with a center frequency of 5.3 GHz and a 1 GHz bandwidth. It is an updated version of the radar described by (Hamran and Langley, 2006), which was optimized to validate the ASAR instrument onboard the EnviSat platform. The unambiguous range in air is 67.4m with 451 samples in the frequency domain. Its two quad-ridged horn antennas are separated by 10 cm and are treated as monostatic. Each trace contains 1024 samples with a time increment of 0.219 ns. The effective time window (after removal of the antenna leakage) is 177 ns, corresponding to a penetration depth of about 20 m in dry polar firn (Fig. 1.11). The nominal vertical resolution in air is 15 cm and 11 cm in a firn pack with relative permittivity ϵ of 1.8, corresponding to a density of 400 kg m^{-3} (Kovacs et al., 1995).

The second radar is an ultra-wide band (UWB) system with a center frequency of 1.75 GHz and a bandwidth of 2.5 GHz. It is the FMCW version of the radar system described in detail by (Ø yan et al., 2010). The unambiguous range in air is 598 m (445 m in firn of $\epsilon = 1.8$) with 10000 samples in the frequency domain. The nominal vertical resolution in air is 6 cm (4.5 cm in firn with $\epsilon = 1.8$). The Vivaldi antennas (Plettemeier et al., 2009) were separated by 0.1 m and we treated them as mono-static. Each trace contains 16384 samples with a time increment of 0.122 ns.

We gated the UWB radar in order to mask the direct wave and improve the contrast between later reflections. The recorded signal is therefore a convolution of the

Fig. 1.1: *C-band (green circle) and UWB radar (yellow circle) mounted on a TL-6 Berco tracked vehicle during the Norwegian-U.S. traverse across East Antarctica.*

transmitter- and receiver-gating signals. Using the same frequency and zero delay on both transmitter and receiver gates results in a window filter with maximum attenuation at time zero, maximum signal strength at the period of the gating frequency, and, again, maximum attenuation for signals arriving at times twice the gating period. We used a gating frequency of 1.0 MHz for the measurements in Antarctica and a gating frequency of 1.523 MHz for the measurements on Svalbard.

Both systems were developed and built at the Norwegian Defence Research Establishment (FFI) supervised by S.E. Hamran.

FMCW data processing

The FMCW radar signal is recorded and sampled in the frequency domain. We applied a window to the raw frequency spectrum to reduce sidelobes after the conversion to the time domain. Only samples in the system's frequency range are stored in order to save memory. It is therefore necessary to add the right amount of zeros before and after the recorded samples to place the spectrum at the correct position along the frequency axis. This step is called zero-padding. We transfer the zero-padded samples to the time domain by an inverse Fast Fourier transform (IFFT). The number of samples used in the IFFT will determine the sample number in the time domain and needs to be chosen adhering to Nyquist to avoid an under-sampling of the signal. After the conversion to

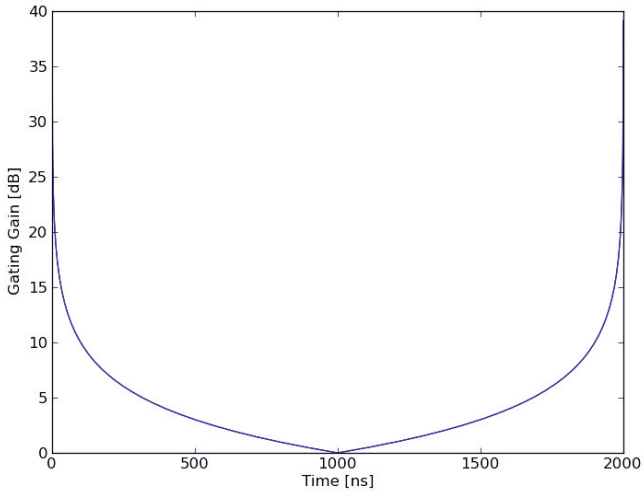

Fig. 1.2: *Spatial filter to remove the gating gain of the UWB radar with a gating frequency of 1 MHz.*

the time domain the signal can be processed using standard methods, such as static correction, averaging, gain, and filtering. Our static correction for the UWB data is 91 samples, corresponding to 11 ns. Static correction removes antenna leakage and the direct wave. The trace interval in our measurements was 0.1 s or 0.2 s. Usual driving speed when measuring was around 2 m s^{-1}. The spatial trace-interval is therefore on the order of 0.2-0.4 m.

We applied three different gain functions depending on the analysis performed. The gating-gain introduced by the system generally provided good contrast. An additional linear gain is applied to enhance the signal from later travel-times where necessary. We intended the phase center to be representative for a SAR measurement (Paper II and III). This required the simulation of a plane wave without gain. Thus, we removed the gating-gain by applying the inverse of the gating filter shown in Fig. 1.2. The spherical wave emitted by the FMCW radar was than flattened by a R^2-gain of the form

$$S(z) \cdot \frac{(h_0 + z)^4}{V(z)} \tag{1.2.15}$$

where

- $S(z)$ is the power of the energy returned from depth z

- h_0 is the antenna height above the surface
- z is the depth below the surface
- $V(z)$ is the volume illuminated by the beam at depth z (eq. 1.2.4).

The GPR data was processed with a collection of scripts that we made public available at `processgpr.sourceforge.net/` (see sec. 2.5).

1.2.4 Synthetic aperture radar

Radar systems operated from on-board air- or spacecrafts transmit a radar signal in side-looking direction and record the portion scattered back towards it (mono-static configuration). The direction along the flight track is called azimuth or along track and the direction perpendicular to it is called range direction or across track (Fig. 1.3). The side-looking geometry is necessary to avoid ambiguities in the range direction due to the extended footprint (Elachi and van Zyl, 2006). The result after SAR processing is a two dimensional image of backscatter strengths from many resolution cells (pixels). The size of each pixel is determined by the range and azimuth resolution of the radar system.

Range resolution is determined by the pulse length (τ_R), which is the inverse of the bandwidth. In order to achieve high range resolution a wide bandwidth is needed. On satellite platforms this is normally realized by a chirp (see sec. 1.2.3).

The azimuth resolution of a real aperture radar is proportional to the range to the target (R), the antenna wavelength (λ) and inversely proportional to the antenna length (D). In other words, high resolution at a remote target requires a very long antenna. A C-band system on board a satellite orbiting the Earth at an altitude of 800 km would need a 1920 m long antenna to achieve a azimuth resolution of 25 m. Synthetic aperture radar (SAR) overcomes this problem by synthesizing a very long antenna by taking advantage of the antenna movement and the resulting Doppler shift. The forward movement during pulse transmission leads to a shift to higher frequencies for targets in the footprint ahead of the radar and to a shift to lower frequencies for targets behind it. This introduces another chirp, which is compressed by a matched filter in the SAR processor. SAR processing requires a coherent system where both amplitude and phase can be measured with high accuracy. The achieved synthetic

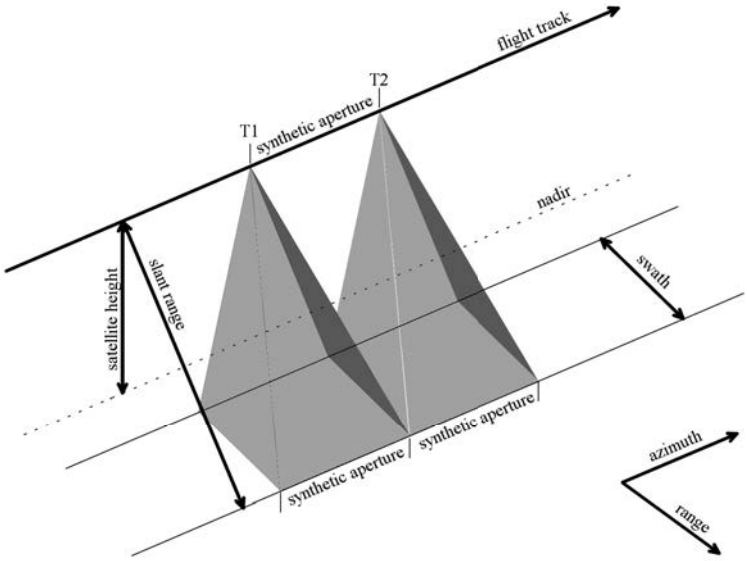

Fig. 1.3: *Sketch of SAR data acquisition at two time intervals T1 and T2. The synthesized aperture covers the distance over which a target is within the radar footprint. Adapted from* `www.sarusersmanual.com`.

azimuth resolution is half the real antenna length ($D/2$). It is independent of R and λ or frequency.

The backscatter strength from a single resolution cell in a SAR image is an average over the individual targets within that cell. It depends on the physical size and electrical properties of the individual targets as well as on the polarization, frequency and incidence angle defined by the system. Weak backscatter is measured over smooth surfaces (relative to the wavelength) or strongly absorbing materials. If a wave impinges on a surface that appears smooth to it at an oblique angle the energy is reflected away from the incident direction at the same angle following Snell's law. Thus, no energy or only an amount indistinguishably from noise is directed back towards the transmitter/receiver system (Fig. 1.4). If the material is strongly absorbing, the incident energy is converted into other forms of energy, such as heat, and lost to the radar system. Strong backscatter occurs over very rough surfaces, heterogeneous volumes, and smooth surface hit at nadir. Over very rough surfaces and after penetration into heterogeneous volumes energy is scattered in all directions and thus also back towards

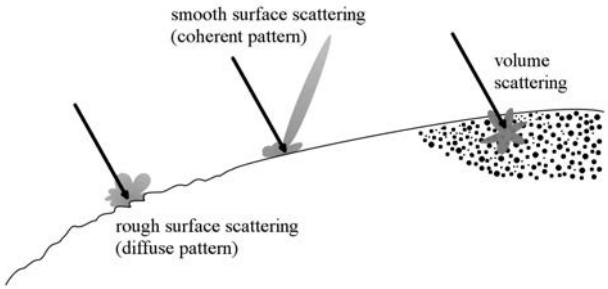

Fig. 1.4: *Different scattering mechanisms on a glacier. Black arrows indicate the incident direction. Parts of the galcier where smooth surfaces scattering dominates appear dark in a SAR image. Areas where rough surface or volume scattering dominate appear bright in a SAR image.*

the antenna. In the special case of a smooth, reflecting surface orientated normal to the incoming wave, all energy not absorbed or transmitted is returned to the antenna.

The returned echo of a radar pulse illuminating a surface or volume is the coherent addition of the single echoes of many scattering points. These add vectorially and result in a single vector of amplitude and phase of the total echo. Since the phase depends on the distance between the radar and target, a slight change in distance will lead to a phase change from all contributing points as well as in a different total amplitude. This variation is called fading (Elachi and van Zyl, 2006). In order to determine the backscatter behavior, many measurements need to be averaged. Similarly, if two neighboring surfaces/volumes have the same σ^0, but different fine details, the returned signal will be different. Thus, an image of a homogeneous surface with a constant σ^0 will show brightness variations from one pixel to the next. This is called speckle. In order to measure the backscatter cross section of the surface/volume, the returns from many neighboring pixels have to be averaged (Elachi and van Zyl, 2006). This processing step is called multi-looking.

We can combine two or more SAR images over the same area with a temporal or spatial antenna offset, called a baseline. This technique is called interferometric SAR or InSAR. The phase difference between the images (a modulo of 2π) contains information

about the surface topography and/or movement. If we use a spatial baseline we can measure topography. If we use temporal baseline we can detect ground movement. If the baseline is temporal and spatial a combination of both is detected and we need to apply corrections if only one is desired.

Topography measurements by InSAR can be biased by penetration into the observed medium (Dall et al., 2001). If the scanned surface allows penetration into the underlying medium, such as over ice or forest, the resulting elevation will deviate from the true surface due to a shift in the target's phase center (see sec. 1.4). The phase difference measured by InSAR is with regard to the target's phase center. If the phase center does not align with the Earth surface the measured elevation will be wrong. Table 1.1 in sec. 1.4.2 gives examples of penetration depths at various frequencies.

1.3 Snow and ice from a microwave perspective

Snow is an aggregate of loosely packed ice crystals. The density of newly fallen snow is 30-150 kg m^{-3} and increases to a maximum of 400-500 kg m^{-3} through metamorphism (Armstrong and Brun, 2008). Snow crusts that occur after refreezing of melted snow can achieve densities of 700-800 kg m^{-3}. It is compacted and transformed under its own weight, and through wind and melt events. Snow that is older than one year is defined as firn (Paterson, 1994). Snow and firn, seen by microwaves, can be described by a mixture of ice and water particles randomly embedded in an air background, where differences in physical properties arise from grain size, bonding and particle volume content. Firn becomes glacier ice when the interconnecting air passages between the grains are sealed off, which occurs at a density of about 830 kg m^{-3} (Paterson, 1994). Air and water pockets might still be present and an increase in ice density results in their compression. Therefore ice can be described as air and water particles randomly embedded in an ice background.

1.3.1 Dielectric properties of snow and ice

The dielectric properties of a medium influencing the propagation of microwaves are the dielectric permittivity (ϵ), the magnetic permeability (μ), and the electrical conductivity (σ). ϵ and μ can be split into an absolute value of $\epsilon_0 = 8.854187 \cdot 10^{-12}$ F m^{-1} and $\mu_0 = 4\pi \cdot 10^{-7}$ NA^{-2} and a relative part (ϵ_r, μ_r) depending on the medium. The refractive index n of a medium is defined as $n = \sqrt{\epsilon_r \mu_r} = c_0 c_{med}^{-1}$ or the ratio of the speed of light and the medium's phase velocity. For most natural media, including snow and ice, which are non-magnetic materials $\mu_r = 1$ and therefore $n = \sqrt{\epsilon_r}$. The dielectric permittivity describes how the electrical properties of a medium influence the passage of the wave. Thus, it is a parameter that indicates the relative (compared to free-space) energy storage capabilities of a dielectric material; the larger its value the greater its ability to store energy (Balanis, 1989). Conductivity describes the tendency for a material to absorb energy from a propagating wave via conversion to other forms of energy, such as heat (Richards, 2008).

Dry snow is a mixture of air and ice. Hence, its relative permittivity is related to the snow density and the relative permittivity of air and ice. The relative permittivity

of ice is 3.15 and is independent of temperature and frequency in the microwave region (Ulaby et al., 1982). Therefore, the relative permittivity of dry snow is governed by the snow density. Density of natural snow packs generally vary over the range of 200-500 kg m^{-3}, which translates to a range of permittivities from 1.37-2.03 (Kovacs et al., 1995). In the case of wet snow, the permittivity becomes an increasing function of the liquid water content in the snowpack.

Radar waves are absorbed in ice by conduction and relaxation. Conduction causes electrons to shift slightly relative to their nuclei, losing energy from the electric field into the host material. Relaxation causes energy to be lost through the oscillation of water molecules. Such absorption is increased in impure ice (high ϵ and σ) and is positively related to temperature (Ulaby et al., 1986).

1.3.2 Physical properties of snow and ice

The physical properties of glacial snow and ice depend on the climatic setting, and thus on the location where on a glacier or ice sheet that the snow is deposited and transformed to firn and ice. We briefly summarize the definitions of the five snow zones given by Paterson (1994) based on the classifications by Benson (1961) and Müller (1962).

In the *dry-snow zone* no melting occurs even in summer. In the *percolation zone* some surface melting occurs and melt-water can percolate some distance into the snow before it refreezes. Ice lenses or glands can form within the snow or firn. The line separating the dry-snow and the percolation zone is called the *dry-snow line*. The boundary to the next zone, the *wet-snow zone* is called the *wet-snow line*. The wet-snow zone is defined as the part where all snow deposited since the end of the previous summer has been raised to 0°C. When sufficient melt-water is produced the ice lenses and glands of the percolation and wet-snow zone will form a continuous mass of ice. The zone where these ice masses are not buried beneath firn is called *superimposed-ice*. The line separating the wet-snow from the superimposed-ice is the *firn line* (or firn edge). It is the boundary between firn and ice on the glacier surface at the end of the melt season. The lower boundary of the superimposed-ice zone is taken as the *equilibrium line*. Above it, the glacier has a net gain over the year and below it a net loss. The zone below the equilibrium line is the *ablation zone*.

Another important form of snow with regard to radar backscatter is *depth hoar*. Depth hoar is low-density firn or snow containing large, faceted, often cup-shaped crystals. Its formation is dependent on rapid crystal growth (Alley, 1988). Rapid growth requires large temperature gradients (order of 10 °C m^{-1}) (Colbeck, 1982). These large gradients are common in late summer or autumn in polar regions when cold air over warm snow causes upward vapor transport (Alley, 1988). In Antarctica, the standard model of firn stratification (Benson, 1962; Gow, 1965) holds that depth hoar is formed in low-density snow at the surface in late summer or autumn, which strong winds in winter cover with fine-grained, high density wind slabs. The standard model interprets each depth-hoar/wind-slab couplet, with or without iced crust, as the autumn and winter of one year (Alley, 1988). However, where snow accumulation is high, depth hoar can form at the bottom of the winter snowpack when the temperature gradient between cold surface air and the bottom of the snowpack is large enough (J.-O. Hagen, pers. comm.).

1.4 Microwave penetration depth

A radar return from a medium includes scattering from its surface, scattering from internal inhomogeneities, and from the interface to the underlying medium. In surface scattering, the scattering strength is proportional to the relative complex dielectric contrasts between embedded inhomogeneities and that of the medium matrix and their density. Its angular scattering pattern is governed by the surface roughness. In volume scattering, the scattering strength is proportional to the dielectric discontinuities inside the medium and the density of the embedded inhomogeneities. The angular volumetric scattering pattern is determined by the roughness of the boundary surface, the average volumetric dielectric constant of the medium, and the geometric size of the inhomogeneities relative to the incident wavelength (Ulaby et al., 1982).

A microwave traveling through a heterogeneous medium, such as snow or ice, experiences losses stemming from two main processes: 1) absorption and 2) scattering. The sum of these losses governs the microwave penetration depth into a medium and is called extinction or attenuation. Absorption occurs if the electrical conductivity of the medium is non-zero. Absorption loss depends on the dielectric properties of the medium and the frequency of the electromagnetic wave. Scattering describes loss in signal strength by mechanisms that distribute energy in other directions than towards the receiver. The main scattering processes are 1) reflection, 2) refraction, and 3) diffraction. Reflection is generally a wanted (and necessary) process in monostatic radar applications, since it first allows us to gain information about a target. Unwanted scatter is termed clutter or noise. Scattering losses depend on the number, size, and distribution of heterogeneities inside a medium and on the contrasts of the dielectric properties between them (Ulaby et al., 1982).

1.4.1 Definitions of penetration depths

Several definitions for penetration depth exist in the literature. The *skin depth* (z_S) of a electrically homogeneous material is defined as the depth over which the strength of the electric field falls to e^{-1} (or 63%) of its original value.

$$z_S = \frac{1}{\alpha}, \tag{1.4.1}$$

where α is the field absorption coefficient (Ulaby et al., 1982). It was originally defined by O. Heaviside in 1885 for the penetration of alternating currents into conductors.

The *power penetration depth* (z_P) of a material is defined as the depth over which the power of the emitted signal has decreased by e^{-1} of its original value. It depends on the total extinction loss rate (absorption and scattering). The extinction per unit length is called the extinction coefficient κ_e $[m^{-1}]$, which can be separated into two parts, namely the absorption coefficient and the scattering coefficient: $\kappa_e = \kappa_a + \kappa_s$ (Ulaby et al., 1982). The power penetration depth is equal to the inverse of the extinction coefficient:

$$z_P = \frac{1}{\kappa_e} \quad . \tag{1.4.2}$$

If no scattering loss is present z_P equals half the skin depth:

$$z_P = \frac{1}{\kappa_a} = \frac{1}{2\alpha} = \frac{z_S}{2} \quad . \tag{1.4.3}$$

The concept of there being a *phase center* (z_ϕ) is rooted in the idealized notion that the radiation field of an antenna is emitted as a spherical wave. Traced back to its apparent origin, the phase center is then the point from which the wave appears to have come (Green, 2008). This concept can be ported to a target, which is treated as the source of a new spherical wave (Huygen's Principle). The phase center of a volume distributed target is the location of its apparent focal position. It is the position in space of a single scatterer equivalent to the combined backscatter from all individual scatterers within the radar-beam. Thus, z_ϕ is a strong function of the target structure (Sarabandi and Lin, 2000).

The elevation bias in an InSAR derived digital elevation model (DEM) or radar altimeter measurement resulting from penetration into a volume scatterer is defined as the difference between the measured elevation and the true surface elevation (Dall, 2007). This bias is equal to the phase center of the returned signal. For example, the scattering-phase center of non-vegetated soil is located at or slightly below the surface, whereas those of vegetated terrain lie at or above the surface, always depending on the dielectric properties of the target and the wavelength applied. The location of

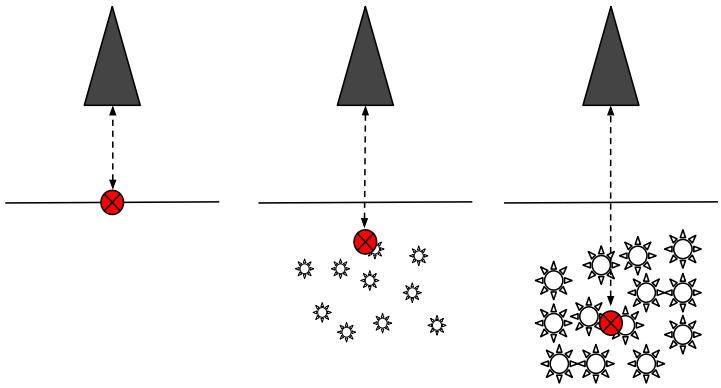

Fig. 1.5: *Illustration of the phase center. The red dot indicates the position of a point target representing volume distributed targets. The phase center is the distance (dashed arrow) from the antenna to that point target. a) Location of the phase center for a single target, which in this case is the boundary between two electrically homogeneous media. The phase center aligns with the target's true location. b) Additional scattering sources below the target drag the phase center towards them. c) The influence on the phase center depends on the scattering cross section of the targets.*

z_ϕ in firn is affected by the number and distribution of individual scatterers and the dielectric contrasts between them. These are the firn layers at L-band (Rott et al., 1993), while single firn grains act as scatterers at Ku-band (Hallikainen et al., 1986). The non-uniform distribution of the physical parameters of the firn layers give rise to inhomogeneous scattering and extinction, which affects the location of z_ϕ.The power penetration depth sets the range in which z_ϕ can be found.

1.4.2 Previous studies on microwave penetration into snow and ice

Rott et al. (1993) derive penetration depth at C- and X-band by means of radiometric transmission measurements on snow blocks and annual brightness temperature measurements by SMMR (Scanning Multichannel Microwave Radiometer). In dry polar firn, they report penetration depths of 21.7 m and 10.4 m for C- and X-band, respectively (Table 1.1). They conclude that in permanently dry firn, areas with high accumulation ($\sim$500 kg m^{-2} a^{-1}) and comparatively homogeneous snow morphology

show low backscatter at C- and X-bands. Pronounced stratification, including depth hoar layers, result in increased backscatter. Davis and Poznyak (1993) analyzed the penetration depth of a X-band pulse radar system in Antarctic firn. Their estimate of the minimum penetration depth at 10 GHz for the cold dry polar plateau region is 4.7 m. Spatial variations in the amount of signal penetration were related to latitude, surface elevation, and mean annual temperature, where they found an increase in penetration depth with increasing latitude and elevation. Dall et al. (2001) compared digital elevation models (DEMs) inferred from air-borne C-band InSAR to an air-borne laser altimeter and GPS surveyed radar reflectors over an ice cap in Greenland. The mean difference measured between laser heights and SAR heights ranged from 0 m in the wet-snow zone to a maximum of 13 m in the percolation zone. Liquid water in the wet-snow zone attenuates the radar energy quickly, prohibiting penetration, while the radar transparency of the dry firn in the percolation zone makes volume scattering dominate at higher elevations. This was the first time the effective phase center of a SAR system was measured directly.

Rignot et al. (2001) compared DEMs inferred from air-borne C-band and L-band InSAR with laser altimeter heights over Greenland and Alaska. The elevation bias (or interferometric depth of the phase center) in cold polar firn on Greenland summit are 9±2 m for C-band and 14±4 m for L-band. Over the surface of Jakobshavn Isbrae, Greenland it is 1±2m for C-band and 3±3 m for L-band except on smooth marginal ice where penetration depth reaches 15±5 m. On colder marginal ice of northeast Greenland, penetration depth reaches 60 to 120 m at L-band. On the temperate ice of Brady and Reid Glacier, Alaska penetration depth is 4±2 m at C-band and 12±6 m at L-band, with little dependence on snow or ice conditions. They conclude that deep penetration is preferable for velocity mapping in order to maintain temporal stability of the radar signal over a long time period. Monitoring changes in glacier volume is probably best addressed by short-wavelength radar.

Dall (2007) showed that the power penetration depth and the elevation bias generally differ in InSAR measurements. The interferometric bias is approximately equal to the two-way power-penetration depth if the latter is small compared to the ambiguity height, which is the topographic height required to introduce one cycle (2π radians) of phase difference. For increasing penetration depth, the bias approaches one quarter of

the ambiguity height. The above mentioned studies are listed in Table 1.1 along with the results from the present thesis for easier comparison.

At frequencies below 10 GHz, z_P is larger for lower densities due to the low absorption and little scattering from snow crystals. Over 20 GHz, the scattering from individual snow crystals in loosely packed snow (low density) is dominating and z_P is larger in denser snow (Surdyk, 2002).

1.4.3 Measuring phase center using GPR

The slope of the unwrapped phase spectrum over the contributing frequency range of the GPR signal is proportional to z_ϕ. We calculate z_ϕ for each trace by the following procedure. First we take the Fourier transform of the time domain signal yielding the amplitude and phase spectrum. The phase spectrum is then unwrapped. In phase unwrapping the 2π cycles are summed up to provide a continuous change in phase. Whenever a 2π jump in phase is encountered 2π is added to or subtracted from the phase. To identify the discontinuities and their sign, the first derivative of the phase is calculated. The slope of the unwrapped phase spectrum is now measured over the frequency range of the GPR (Fig. 1.6):

$$z_\phi = \frac{-\Delta\Phi}{2\Delta k}, \tag{1.4.4}$$

where $\Delta\Phi$ is the phase difference over the given frequency range and $\Delta k = 2\pi f/c$ is the difference in wave number over the same range. The factor 2 in the fraction is due to the two-way travel path.

Uncertainties

Most important, all scatterers contributing to the phase center have to lie within the time window of the GPR. In practice, that means the noise level has to be reached towards the end of th time window. The phase center will always fluctuate around the true value when changing the time window, due to random noise. The selection of the gain applied is important, since it can enhance deeper reflections in an unrealistic manner. Proper phase unwrapping requires sufficient frequency samples. Too few samples will result in cycle jumps, which will decrease the slope $\Delta\phi/\Delta f$ and therewith the phase center. We found 2^{15} samples in the FFT to be sufficient for the C-band and

Table 1.1: *Studies on microwave penetration into snow and ice.* * z_P *measured as transmission (one-way) opposed to reflection (two-ways).* $^\#$ *Measured thickness of snow bridges over crevasses.*

Location	z [m]	f [GHz]	Comment	Reference
Antarctic plateau	8.1	10.3	$z_P{}^*$	Rott et al. (1993)
Antarctic plateau	21.7	5.2	$z_P{}^*$	Rott et al. (1993)
Antarctic plateau	35-45	1.75	z_ϕ	Paper II
Lake Vostok, Antarctica	>4.7	10.0	$z_P{}^\#$	Davis and Poznyak (1993)
Coastal DML, Antarctica	17.5±2.9	1.75	z_ϕ	Paper II
Fimbulisen, Antarctica	9.6±0.8	1.75	z_ϕ	Paper II
Amery ice shelf, Antarctica	5.7±1.2	13.2	$z_P{}^\#$	Lacroix et al. (2007)
Greenland, dry snow zone	27	5.3	$z_P{}^*$	Hoen and Zebker (2000)
Ryder glacier, Greenland	20	5.3	$z_P{}^*$	Hoen and Zebker (2000)
Geikie ice cap, Greenland	13	5.2	z_ϕ	Dall et al. (2001)
Greenland, cold marginal ice	60-120	1.2	z_ϕ	Rignot et al. (2001)
Brady glacier, Alaska	12±6	1.2	z_ϕ	Rignot et al. (2001)
Brady glacier, Alaska	4±2	5.3	z_ϕ	Rignot et al. (2001)
Kongsvegen glacier, Svalbard	12.0±4.3	1.2	z_ϕ	Paper III
Kongsvegen glacier, Svalbard	3.7±2.1	2.5	z_ϕ	Paper III
Kongsvegen glacier, Svalbard	3.5±2.1	5.3	z_ϕ	Paper III

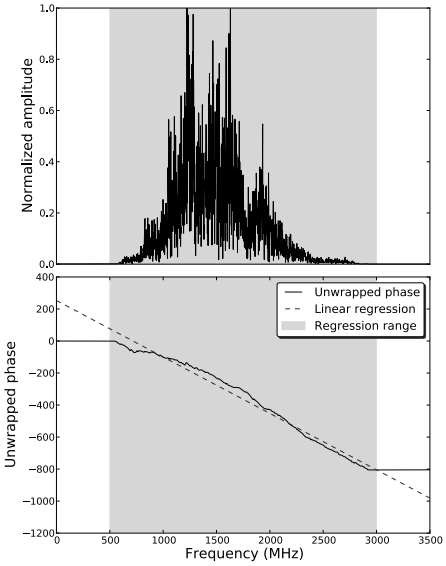

Fig. 1.6: *Illustration on how to calculate the phase center. A linear regression is fitted to the unwrapped phase over the full frequency range 0.5-3 GHz. The slope of the regression line multiplied by $c_0/(4\pi)$ is the phase center. There is a difference in slope between the lower and higher frequencies. Another valid approach would be to determine the slope of the regression only over frequencies dominating the amplitude spectrum. A window function was applied to the spectrum to reduce side-lobes, therefore the distribution of frequencies is misleading.*

UWB radar traces. Higher amounts of samples did not change the value of the phase center, but increased computing demands (Fig. 1.7). System noise (antenna leakage) has to be removed prior to the FFT. The broad bandwidth can lead to a change in slope of the unwrapped phase spectrum. Lower frequencies have steeper slopes, which correspond to deeper z_ϕ. The opposite is true for higher frequencies (Fig. 1.6).

1.4.4 Estimating power penetration depth

In order to obtain an estimate for z_P, we consider an electromagnetic wave incident upon the snow surface from air in direction z. Here, part of its energy is scattered back into the air, while most of it will penetrate into the snow volume. In the case of dry polar snow, the Fresnel reflection coefficient is on the order of 0.02 at nadir (Ulaby et al., 1982), meaning that about 98% of the power is transmitted across the air-snow

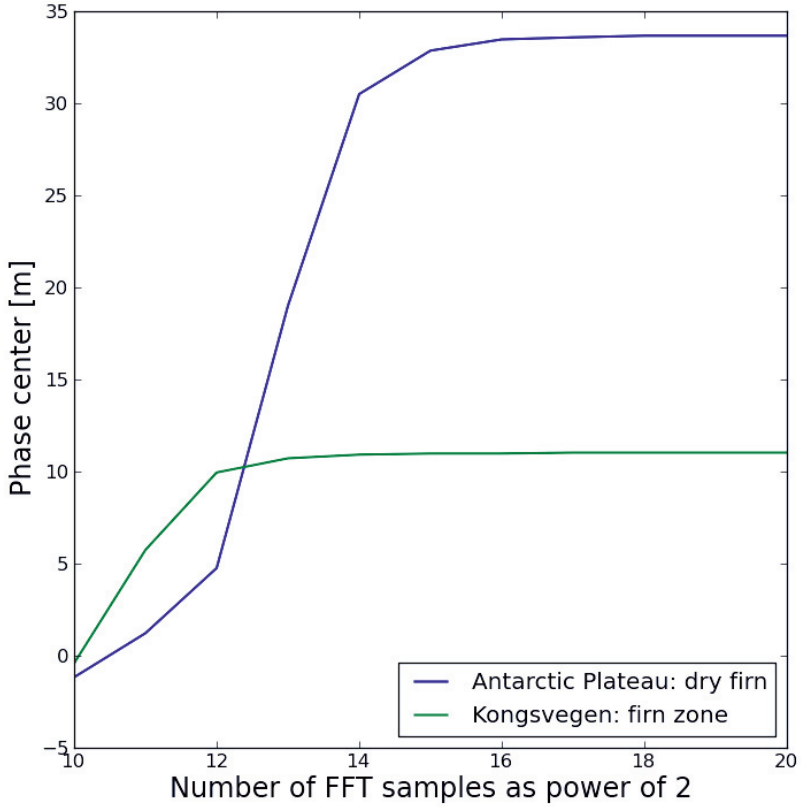

Fig. 1.7: *Number of FFT samples in the spectrum analysis versus the calculated phase center in meter. Undersampling introduces cycle slips that lead to a too shallow phase center. A very high number of samples increases computing demands. We found 2^{15} samples to be a good compromise between computing efficiency and accuracy. The blue line is from the central East Antarctic Plateau (21.9° E, -84.8° N) representing an area where we have the deepest phase centers. The green line is from the higher firn zone on Kongesvegen, Svalbard (13.2° E, 78.8° N)*

boundary. If the transmitted power at a point just beneath the surface ($z = 0+$) is $P(0+)$, the power at depth z is given by

$$P(z) = P(0+)e^{\left(-\int_0^z \kappa_e(z')dz'\right)} \quad , \tag{1.4.5}$$

where $\kappa_e(z)$ is the power extinction coefficient of the medium at depth z. The power penetration depth z_P can then be determined by the following equation

$$\frac{P(z_P)}{P(0+)} = \frac{1}{e} \quad . \tag{1.4.6}$$

We estimate z_P within the snow by measuring the power decay along a GPR trace. The energy recorded at the receiver has traveled down and up within the snowpack. Thus, we only can measure the effective z_P over the range of the GPR defined by the set time-window.

We convert the two-way travel-time (TWT) to depth by

$$z = \frac{TWT}{2} c_{med} \quad , \tag{1.4.7}$$

assuming a constant medium velocity c_{med}.

We approximate the total backscattered power P^{σ}_{total} by integrating along a trace down to the noise floor, z_{noise}

$$P^{\sigma}_{total} = \int_0^{z_{noise}} P_r(z)dz \quad . \tag{1.4.8}$$

$P_r(z)$ is the received power from depth z from equation 1.2.6. Further, we approximate the power of the energy returned from above a specific depth z_i by

$$P^{\sigma}(< z_i) = \int_0^{z_i} P_r(z)dz \quad . \tag{1.4.9}$$

Thus, the remaining power that can be returned from below z_i is

$$P^{\sigma}(> z_i) = \int_{z_i}^{z_{noise}} P_r(z)dz = P^{\sigma}_{total} - P^{\sigma}(< z_i) \quad . \tag{1.4.10}$$

We calculate z_P as the depth z_i where

$$\frac{P^{\sigma}(> z_i)}{P^{\sigma}_{total}} = 1 - \frac{P^{\sigma}(< z_i)}{P^{\sigma}_{total}} = e^{-1} \quad . \tag{1.4.11}$$

Fig. 1.8 illustrates the procedure.

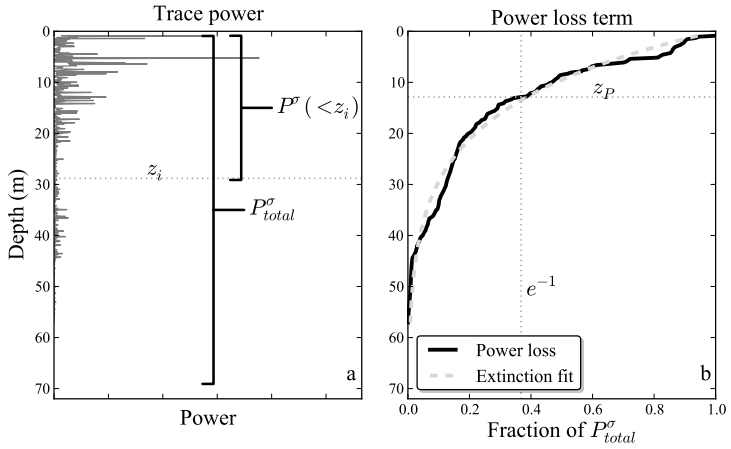

Fig. 1.8: *Illustration on how to estimate z_P. a) Total backscattered power P^{σ}_{total} is the sum along the whole trace and the power backscattered from a specific depth $P^{\sigma}(z_i)$ is the sum along the trace down to that depth. b) The difference between P^{σ}_{total} and $P^{\sigma}(< z_i)$ is the is the remaining power to be returned from below z_i. z_P is the depth where the loss curve has dropped by e^{-1}.*

1.4.5 Effects of the different viewing geometries between GPR and SAR

The GPR sends out a spherical wave, which is directed towards the air-snow interface by the antenna. Thus, the EM wave impinges on the air-snow interface at nadir. In the case of SAR, the wave will impinge on the air-snow interface at an angle, typically 10°-60°. This is to avoid range ambiguities. The typically long distance between antenna and target and the SAR processing itself produce a plane wave impinging on the interface. In a plane wave the surfaces of constant phase are parallel, while they are curved in the spherical case. In practise this means that, a spherical wave, impinging on a horizontal interface has different phase and amplitude at two neighboring points on the interface at a given time instance. In addition, a spherical wave is multi-directional, while a plane wave is unidirectional (Fig. 1.9).

Differences in the backscatter observed by GPR and SAR are mostly related to horizontal, smooth interfaces, leading to specular reflections. They give high GPR backscatter, but very low SAR backscatter, because energy is reflected away from the sensor in the latter case. Volume scattering at randomly orientated scatterers will

not be influenced by the incidence direction or shape of the incoming wave. In the case of orientated targets, backscatter will depend on incident direction and thus the look-direction of the SAR.

Baumgartner et al. (2002) found that differences between ground-based and space-borne derived normalized radar cross section increase as 1) the range for the ground-based radar decreases, and 2) the extinction coefficient (which effects penetration depth) is decreased. However, their findings are based on a homogeneous half-space model, where no scattering occurs and the absorption coefficient does not vary with depth.

We apply an R^2 gain to the GPR data to compensate for the spherical spreading of the wave front. This will simulate the amplitudes of a plane wave. Variations in backscatter due to differences in incidence direction can not be corrected. Snow or firn is generally isotropic and volume scattering from snow or firn is therefore direction independent. If strong vertical vapor transport exists in response to atmospheric forcing a vertical anisotropy exists in the upper 2-5 m in polar firn (Alley, 1988). However, this anisotropy exists on the snow crystal scale and C-band and especially L-band frequencies will not resolve it.

The penetration depth is defined as the path length traveled inside the medium up to the point when the power has decayed by e^{-1} of its original value. For the nadir-looking GPR this length is equal to the vertical depth below the surface. For SAR the oblique look-angle has to be taken into account. The penetration depth in the propagation direction (l) is related to the vertical depth (d) by

$$d = l \cdot \cos\theta_1, \tag{1.4.12}$$

where θ_1 is the incidence angle after refraction into the medium. If the refractive index of the snowpack is low, θ_1 stays approximately equal to the incident angle.

1.5 Study sites

The radar data for this thesis were collected in different polar environments, Dronning Maud Land (DML) in East Antarctica and Northwestern Svalbard. DML covers the sector of Antarctica facing South Africa. Monthly mean temperatures for the ice

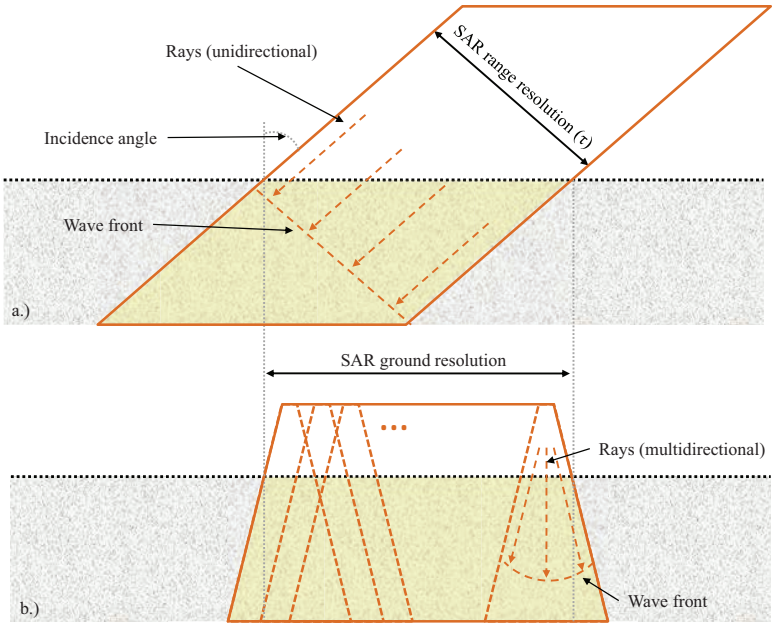

Fig. 1.9: *(a) Schematic of the effective scattering volume for a single SAR resolution cell. Note that the area contributing to the signal changes depending on the angle of incidence of the beam. Greater incident angles approach the vertical depth integration employed for the GPR. This image is correct for the situation where the GPR is profiling in the SAR range direction. (b) Equivalent GPR effective beam area. Energy radiated from the two systems is incident on potential scattering sources at different angles. SAR is effectively unidirectional while the GPR radiates out from the source within the limits of the beam area. Adapted from Langley et al. (2007).*

shelves in DML range from -2°C to -15°C. Monthly mean temperatures for the ice sheet in DML range from -17°C to -46°C (Comiso, 2000). The mean summer and winter 7 m wind speeds in DML are generally below 5 m s^{-1} (Van Lipzig et al., 2004). The amplitude of the annual cycle of precipitation is on the order of 5 mm w.e. for DML (Marshall, 2009). The interior of DML is a dry-snow zone (roughly above 2000 m a.s.l.). The margins represent the percolation and wet-snow zones. Ablation does not occur and mass is only lost by calving and some melting at the base (Paterson, 1994). In East Antarctica, our GPR profiles range from the coast on Fimbulisen to the South Pole. Thus, they cover the wet snow, the percolation, and the dry snow zones.

Svalbard is an archipelago in the Barents Sea between Greenland and the Russian Arctic. It is situated in a warmer more maritime climate compared to the sites visited in Antarctica. Arctic glaciers, such as on Svalbard seldom have a dry-snow zone. GPR measurements on Kongsvegen glacier, Svalbard yield data from the percolation, wet-snow, superimposed-ice, and ablation zone (see section 1.3). With these datasets we were able to investigate the radar response from snow and ice under various climatic settings.

1.5.1 Norwegian - US Scientific Traverse across East Antarctica

Data for this thesis were collected during the Norwegian-U.S. Scientific Traverse across East Antarctica (`http://traverse.npolar.no`).

The traverse was conducted in two stages in austral summers 2007/2008 and 2008/2009. The first stage headed out from the Norwegian research station Troll along the main ice divide via Plateau Station and the Pole of Inaccessibility towards South Pole (Goldman, 2008) (Fig. 1.10). Equipment overwintered 350 km north of South Pole Station from where the second stage started in the following season. In the second year, the traverse traveled to South Pole and returned via the Recovery Lakes and Kohnen station to Troll (Fig. 1.10). Elevations between 30 m a.s.l. at the edge of Fimbulisen to 3725 m a.s.l. at the Pole of Inaccessibility were covered. Most of the areas covered by the traverse experience very little annual snow accumulation (Müller et al., 2010; Anschütz et al., 2009; Arthern et al., 2006).

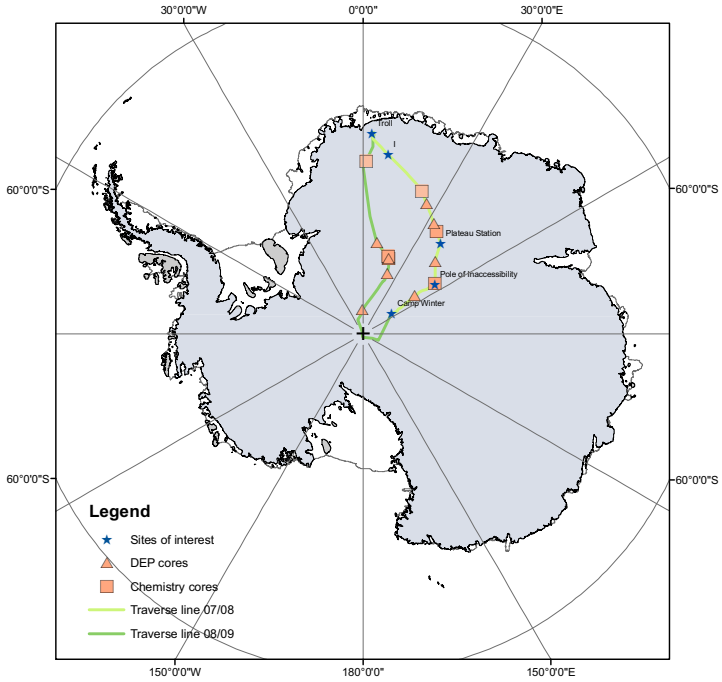

Fig. 1.10: *The route of the Norwegian-U.S. scientific traverse 2007-2009 drawn on a map of Antarctica.*

Firn cores, snow samples, and continuous GPR and GPS data were acquired during the traverse. Most relevant for this thesis are the datasets from the C-band and the UWB GPR systems, as well as the shallow firn cores (Anschütz et al., 2009). The C-band radar was utilized both seasons with a profile length exceeding 5000 km. An 860 km long section from the first stage is used for surface mass-balance studies in Paper I calibrated by five shallow firn cores. The newly developed UWB system was only available for the return route from South Pole to Troll in 2008/2009. Parts of the UWB radar data are used in Paper II.

1.5.2 Kongsvegen glacier on Svalbard

Kongsvegen is a 25 km long glacier situated in Northwestern Svalbard close to the research station Ny-Ålesund (Fig. 1.12). It is a polythermal glacier with a cold ice zone in the ablation area and temperate ice (ice close to the pressure melting point) in the accumulation area and deeper ablation area. The glacier is continuously monitored since 1986 using a network of stakes, snow-pits and GPR measurements along its centerline (Hagen et al., 2005, 1999; Liestø l, 1988).

Surveys with the C-band radar have been made in April 2004, 2005, and 2006 (Langley et al., 2008). The UWB was used in 2008 (Hamran et al., 2009) (Fig. 1.13). These datasets were available to us and used in the studies in Papers II and III.

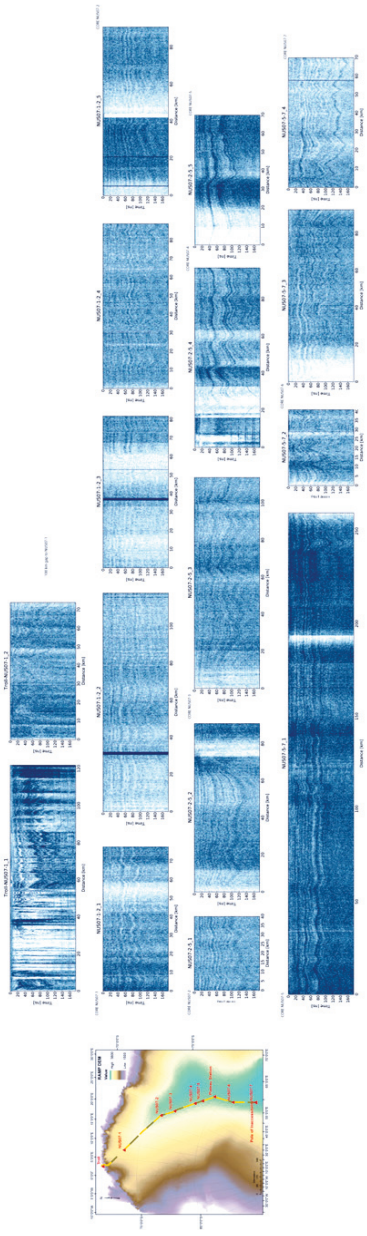

Fig. 1.11: *C-band GPR profile from stage one of the Nowegian-US scientific traverse.*

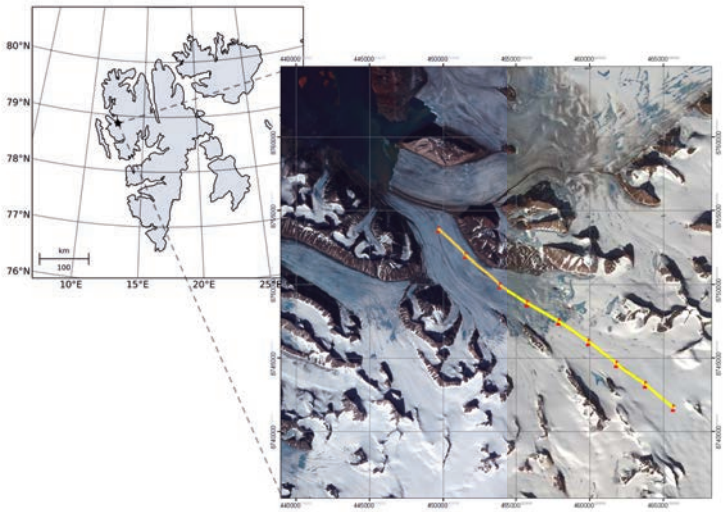

Fig. 1.12: *Aster image from 01.08.2009 over Kongsvegen glacier and surrounding. The yellow line indicates the GPR profile along the centerline and the red flags mark the positions of the mass-balance stakes, both for the year 2008. The ablation area below stake 5 can be clearly seen.*

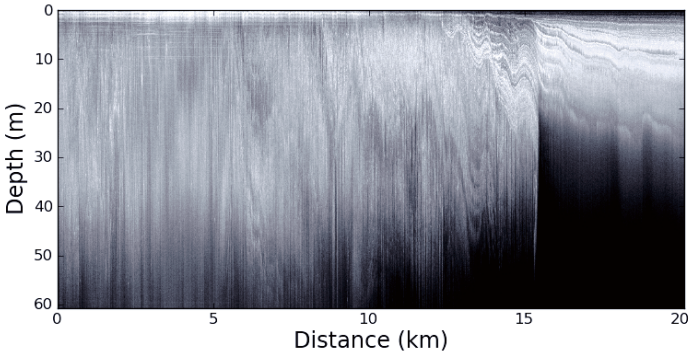

Fig. 1.13: *UWB profile along Kongsvegen's centerline between stakes 1 and 9 (yellow line in Fig. 1.12).*

References

Alley, R. B. (1988). Concerning the deposition and diagenesis of strata in polar firn. *Journal of Glaciology*, 34(118):283–290.

Alley, R. B., Clark, P. U., Huybrechts, P., and Joughin, I. (2005). Ice-Sheet and Sea-Level Changes. *Science*, 310(5747):456–460.

Anschütz, H., Müller, K., Isaksson, E., McConnell, J. R., Fischer, H., Miller, H., Albert, M. R., and Winther, J.-G. (2009). Revisiting sites of the South Pole Queen Maud Land Traverses in East Antarctica: Accumulation data from shallow firn cores. *J. Geophys. Res.*, 114(D24):D24106—-.

Arcone, S. A., Spikes, V. B., and Hamilton, G. S. (2005). Stratigraphic variation within polar firn caused by differential accumulation and ice flow: interpretation of a 400 MHz short-pulse radar profile from West Antarctica. *Journal of Glaciology*, 51:407–422.

Armstrong, R. L. and Brun, E., editors (2008). *Snow and Climate: Physical Processes, Surface Energy Exchange and Modeling*. Cambridge University Press.

Arthern, R. J., Winebrenner, D. P., and Vaughan, D. G. (2006). Antarctic snow accumulation mapped using polarization of 4.3-cm wavelength microwave emission. *Journal of Geophysical Research*, 111, D0610.

Balanis, C. A. (1989). *Advanced Engineering Electromagnetics*. John Wiley & Sons.

Baumgartner, F., Munk, J., Jezek, K. C., and Gogineni, S. (2002). On Reconciling Ground-Based With Spaceborne Normalized Radar Cross Section Measurements. *Geoscience and Remote Sensing, IEEE Transactions on*, 40(2):494–496.

Benson, C. S. (1961). Stratigraphic studies in the snow and firn of the Grennland Ice Sheet. *Folia Geographica Danica*, 9:13–37.

Benson, C. S. (1962). Stratigraphic studies in the snow and firn of the Greenland ice sheet. Technical Report 70, SIPRE Res. Rep.

Bingham, A. W. and Drinkwater, M. R. (2000). Recent changes in the microwave scattering properties of the Antarctic ice sheet. *Geoscience and Remote Sensing, IEEE Transactions on*, 38(4):1810–1820.

Bogorodsky, V. V., Bentley, C. R., and Gudmandsen, P. E. (1985). *Radioglaciology*. Springer.

Brooks, R. L., Campbell, W. J., Ramseier, R. O., Stanley, H. R., and Zwally, H. J. (1978). Ice sheet topography by satellite altimetry. *Nature*, 274(5671):539–543.

Colbeck, S. C. (1982). An overview of seasonal snow metamorphism. *Rev. Geophys.*, 20(1):45–61.

Comiso, J. C. (2000). Variability and trends in Antarctic surface temperatures from in situ and satellite infrared measurements. *Journal of Climate*, 13:1674–1696.

Dall, J. (2007). InSAR elevation bias caused by penetration into uniform volumes. *Geoscience and Remote Sensing, IEEE Transactions on*, 45(7):2319–2324.

Dall, J., Madsen, S. N., Keller, K., and Forsberg, R. (2001). Topography and penetration of the Greenland Ice Sheet measured with airborne SAR Interferometry. *Geophys. Res. Lett.*, 28(9):1703–1706.

Daniels, D. J., editor (2004). *Ground Penetration Radar*. The Institution of Electrical Engineers, London, 2nd editio edition.

Davis, C. H. and Poznyak, V. I. (1993). The depth of penetration in Antarctic firn at 10 GHz. *Geoscience and Remote Sensing, IEEE Transactions on*, 31(5):1107–1111.

Eisen, O. and Others, . (2008). Ground-based measurements of spatial and temporal variability of snow accumulation in East Antarctica. *Reviews of Gephysics*, 46, RG2001.

Elachi, C. and van Zyl, J. (2006). *Introduction to the physics and techniques of remote sensing*. Wiley, 2nd edition.

Engeset, R. V., Kohler, J., Melvold, K., and Lundén, B. (2002). Change detection and monitoring of glacier mass balance and facies using ERS SAR winter images over Svalbard. *International Journal of Remote Sensing*, 23(10):2023–2050.

Fujita, S., Maeno, H., Uratsuka, S., Furukawa, T., Mae, S., Fujii, Y., and Watanabe, O. (1999). Nature of radio echo layering in the Antarctic Ice Sheet detected by a two-frequency experiment. *Journal of Geophysical Research*, 104(B6):13,01313,024.

Goldman, H. V. (2008). From the editor: halfway through the IPY - halfway for an Antarctic traverse. *Polar Research*, 27:1–6.

Gow, A. J. (1965). Snow studies in Antarctica. Research report 177, CRREL Res. Rep.

Green, H. E. (2008). The phase centre of a pure mode, smooth wall, conical horn. *Progress In Electromagnetics Research*, 4:285–298.

Hagen, J. O., Eiken, T., Kohler, J., and Melvold, K. (2005). Geometry changes on Svalbard glaciers: mass-balance or dynamic response? *Annals of Glaciology*, 42:255–261(7).

Hagen, J.-O., Melvold, K., Eiken, T., Isaksson, E., and Lefauconnier, B. (1999). Mass balance methods on Kongsvegen, Svalbard. *Geogr. Ann.*, 81 A(4):593–601.

Hallikainen, M., Ulaby, F., and Abdelrazik, M. (1986). Dielectric properties of snow in the 3 to 37 GHz range. *IEEE Transactions on Antennas and Propagation*, 34(11):1329–1340.

Hamran, S.-E. and Langley, K. (2006). C-band Polarimetric GPR. In *11th International Conference on Ground Penetrating Radar*.

Hamran, S. E., Ø yan, M. J., and Kohler, J. (2009). UWB radar profiling reveals glacier facies. In *Proceedings IWAGPR*.

Hoen, W. E. and Zebker, H. A. (2000). Penetration depths inferred from interferometric volume decorrelation observed over the Greenland Ice Sheet. *Geoscience and Remote Sensing, IEEE Transactions on*, 38(6):2571–2583.

Hulbe, C. L., Scambos, T. A., Youngberg, T., and Lamb, A. K. (2008). Patterns of glacier response to disintegration of the Larsen B ice shelf, Antarctic Peninsula. *Global and Planetary Change*, 63(1):1–8.

Jenkins, A. and Doake, C. S. M. (1991). Ice-Ocean Interaction on Ronne Ice Shelf, Antarctica. *J. Geophys. Res.*, 96(C1):791–813.

Jezek, K. C. and Team, R. P. (2002). RAMP AMM-1 SAR Image Mosaic of Antarctica. Fairbanks, AK: Alaska SAR Facility, in association with the National Snow and Ice Data Center.

Kohler, J., James, T. D., Murray, T., Nuth, C., Brandt, O., Barrand, N. E., Aas, H. F., and Luckman, A. (2007). Acceleration in thinning rate on western Svalbard glaciers. *Geophys. Res. Lett.*, 34(18):L18502—-.

König, M., Winther, J.-G., Knudsen, N. T., and Guneriussen, T. (2001). Firn-line detection on Austre-Okstindsbreen, Norway, with airborne multipolarization SAR. *Journal of Glaciology*, 47(157):251–258.

Kovacs, A., Gow, A. J., and Morey, R. M. (1995). The in-situ dielectric constant of polar firn revisited. *Cold Regions Science and Technology*, 23(3):245–256.

Lacroix, P., Legresy, B., Coleman, R., Dechambre, M., and Remy, F. (2007). Dual-frequency altimeter signal from Envisat on the Amery ice-shelf. *Remote Sensing of Environment*, 109(3):285–294.

Langley, K., Hamran, S.-E., Hø gda, K.-A., Storvold, R., Brandt, O., Hagen, J.-O., and Kohler, J. (2007). Use of C-Band Ground Penetrating Radar to Determine Backscatter Sources Within Glaciers. *Geoscience and Remote Sensing, IEEE Transactions on*, 45(5).

Langley, K. A., Hamran, S.-E., Hø gda, K. A., Storvold, R., Brandt, O., Kohler, J., and Hagen, J.-O. (2008). From Glacier Facies to SAR Backscatter Zones via GPR. *Geoscience and Remote Sensing, IEEE Transactions on*, 46(9):2506–2516.

Liestø l, O. (1988). The glaciers in the Kongsfjorden area, Spitsbergen. *Det Norske Geografiske Tidsskrifte*, 42:231–238.

MacGregor, J. A., Winebrenner, D. P., Conway, H. B., Matsuoka, K., Mayewski, P. A., and Clow, G. D. (2007). Modeling englacial radar attenuation at Siple Dome, West Antarctica, using ice chemistry and temperature data. *J. Geophys. Res.*, 112.

Marshall, G. J. (2009). On the annual and semi-annual cycles of precipitation across Antarctica. *International Journal of Climatology*, 29(15):DOI: 10.1002/joc.1810.

Marshall, H.-P. and Koh, G. (2008). FMCW radars for snow research. *Cold Regions Science and Technology*, 52(2):118–131.

Matsuoka, K., Morse, D., and Raymond, C. F. (2010). Estimating englacial radar attenuation using depth profiles of the returned power, central West Antarctica. *J. Geophys. Res.*, 115(F2):F02012—-.

Müller, F. (1962). Zonation in the accumulation area of the glaciers of Axel Heiberg Island, NWT, Canada. *Journal of Glaciology*, 4(33):302–311.

Müller, K., Sinisalo, A., Anschütz, H., Hamran, S. E., Hagen, J. O., McConnell, J. R., and Pasteris, D. R. (2010). An 860 km surface mass-balance profile on the {E}ast {A}ntarctic plateau derived by {GPR}. *Annals of Glaciology*, 51(55):1–8.

Murray, T., Stuart, G. W., Miller, P. J., Woodward, J., Smith, A. M., Porter, P. R., and Jiskoot, H. (2000). Glacier surge propagation by thermal evolution at the bed. *J. Geophys. Res.*, 105(B6):13491–13507.

Ø yan, M. J., Hamran, S. E., Hanssen, L., Berger, T., and Plettemeier, D. (2010). Ultra Wideband Gated Step Frequency Ground Penetrating Radar. *Geoscience and Remote Sensing, IEEE Transactions on*, submitted.

Paterson, W. S. B. (1994). *The physics of glaciers*. Pergamon, 3rd edition.

Plettemeier, D., Ciarletti, V., Hamran, S.-E., Corbel, C., Cais, P., Benedix, W.-S., Wolf, K., Linke, S., and Roddecke, S. (2009). Full polarimetric GPR antenna system aboard the ExoMars rover. In *Radar Conference, 2009 IEEE*, pages 1–6.

Rees, W. G. (2006). *Remote sensing of snow and ice*. Taylor and Francis, Philadelphia, Pa.

Richards, J. A. (2008). *Radio Wave Propagation*. Springer.

Richardson, C., Hamran, S. E., Holmlund, P., Isaksson, E., and Aarholt, E. (1997). Spatial distribution of snow in western Dronning Maud Land, East Antarctica, mapped by a ground-based snow radar. *Journal of Geophysical Research*, 102(B9):20343–20353.

Rignot, E. (2008). Changes in West Antarctic ice stream dynamics observed with ALOS PALSAR data. *Geophys. Res. Lett.*, 35(12):L12505.

Rignot, E., Echelmeyer, K., and Krabill, W. (2001). Penetration depth of interferometric synthetic-aperture radar signals in snow and ice. *Geophys. Res. Lett.*, 28(18):3501–3504.

Rignot, E. and Thomas, R. H. (2002). Mass Balance of Polar Ice Sheets. *Science*, 297(5586):1502–1506.

Rotschky, G., Rack, W., Dierking, W., and Oerter, H. (2006). Retrieving snowpack properties and accumulation estimates from a combination of SAR and scatterometer measurements. *IEEE Transactions on Geoscience and Remote Sensing*, 44(4):943–956.

Rott, H., Cline, D., Duguay, C., Essery, R., Haas C.an Macelloni, G., Malnes, E., Pulliainen, J., Rebhan, H., and Yueh, S. (2008). CoReH2O - A Ku- and X-Band SAR Mission for Detailed Studies of Snow and Ice Processes. In *Proc. of 7th EUSAR Conf.*, volume 2, pages 111–114.

Rott, H., Sturm, K., and Miller, H. (1993). Active and passive microwave signatures of Antarctic firn by means of field measurements and satellite data. *Annals of Glaciology*, 17:337–343.

Sarabandi, K. and Lin, Y.-C. (2000). Simulation of interferometric SAR response for characterizing the scattering phase center statistics of forest canopies. *Geoscience and Remote Sensing, IEEE Transactions on*, 38(1):115–125.

Scambos, T., Fricker, H. A., Liu, C.-C., Bohlander, J., Fastook, J., Sargent, A., Massom, R., and Wu, A.-M. (2009). Ice shelf disintegration by plate bending and hydro-fracture: Satellite observations and model results of the 2008 Wilkins ice shelf break-ups. *Earth and Planetary Science Letters*, 280(1-4):51–60.

Surdyk, S. (2002). Using microwave brightness temperature to detect short-term surface air temperature changes in Antarctica: An analytical approach. *Remote Sensing of Environment*, 80(2):256–271.

Ulaby, F. T., Moore, R. K., and Fung, A. K., editors (1981). *Microwave remote sensing: Active and Passive*, volume 1

of *Remote Sensing*. Addison-Wesley.

Ulaby, F. T., Moore, R. K., and Fung, A. K., editors (1982). *Microwave Remote Sensing: Active and Passive*, chapter Physical m. Addison-Wesley Publishing Company.

Ulaby, F. T., Moore, R. K., and Fung, A. K., editors (1986). *Microwave remote sensing: Active and Passive*, volume 3 of *Remote Sensing*. Addison-Wesley.

Van Lipzig, N. P. M., Turner, J., Colwell, S. R., and den Broeke, M. R. (2004). The near-surface wind field over the Antarctic continent. *International Journal of Climatology*, 24:1973–1982.

Chapter 2

Summary of papers

2.1 Paper I

An 860 km surface mass-balance profile on the East Antarctic plateau derived by GPR, Karsten Müller, Anna Sinisalo, Helgard Anschütz, Svein-Erik Hamran, Jon-Ove Hagen, Joseph R. McConnell, Daniel R. Pasteris. *Annals of Glaciology*, 2010, vol. 51, no. 55.

This paper presents the surface mass balance (SMB) along an 860 km section of the Norwegian-U.S. scientific traverse across East Antarctica. We used GPR reflection horizons, representing isochronous firn layers, to infer the snow accumulation rate. Five shallow firn cores were tie points to the GPR for calibration and identification of dated firn layers. The firn cores were analyzed by the Norwegian Polar Institute using dielectric profiling (DEP). Acid ash deposited after major volcanic eruptions from around the world leads to a significant increase in the electrical conductivity reading in the DEP. These anomalies are used to establish a time-depth table, which is used to calculate the average accumulation rate since a volcanic event. Average accumulation rates can be measured with high accuracy along firn cores, but they say little about the spatial variability of the accumulation rate.

We used the GPR profiles recorded with the C-band FMCW radar to study the SMB variability. We analyzed all data from the first stage of the traverse and used the profiles that permitted a clear identification of reflection horizons at the maximum depth of the Tambora layer, identified in the DEP analysis. Gaps in the GPR data

stem from problems with the power supply of the system, a short circuit in the antenna, and too cold temperatures. North of the chosen profile the Tambora layer lies deeper than 20 m and therewith outside of the applied GPR time window.

We derive a 200 year mean surface mass balance of 23.7 kg m^{-2} a^{-1} along the profile, estimating the maximum error to be 3.1 kg m^{-2} a^{-1}. The SMB decreases with a rate of 1.3 kg m^{-2} a^{-1} per 100 km southwards along the profile with increasing elevation and continentality. Our values are significantly lower than those reported in the literature for this region. Reasons for this can be different time-spans or the lack of in-situ measurements in the large scale studies, which rely on interpolation schemes. We attempted to extrapolate our SMB estimates using EnviSat ASAR images over the region to investigate the influence of averaging in large scale studies. Though this is not directly part of the paper, a detailed description may be found in chapter 5.

2.2 Paper II

Phase-center of L-band radar in polar snow and ice, Karsten Müller, Svein-Erik Hamran, Anna Sinisalo, Jon-Ove Hagen. *IEEE Transactions on Geoscience and Remote Sensing, in press.*

Microwave remote sensing from space allows us to monitor large parts of the polar regions with good spatial and temporal coverage. Over impenetrable surfaces the physical and dielectric properties of that surface are required to interpret the return signal correctly. When the wave penetrates into the medium, the internal structure must also be taken into account. We investigate the phase center z_ϕ as the distance to the apparent surface reflection from within a snowpack at several sites in Antarctica and on an Arctic glacier. We calculate z_ϕ from our UWB radar over the frequency range of 0.5-3 GHz and find that z_ϕ is deepest in dry Antarctic firn (z_ϕ >40 m). In firn that exhibits a uniform scattering pattern over depth, z_ϕ correlates with the depth to the firn-ice transition. A deeper firn-ice transition corresponds to a deeper z_ϕ. Melt-layers in snow or firn, varying air bubble content in glacier ice or alternating firn and ice layers can form clusters of increased backscattering in a volume of snow or ice. These clusters of relatively higher backscatter will pull z_ϕ towards them.

2.3 Paper III

Change in microwave scattering mechanisms along Kongsvegen glacier, Svalbard and implications for SAR monitoring, Karsten Müller, Svein-Erik Hamran, Anna Sinisalo, Jon-Ove Hagen. *in prep.*

In this paper we compare GPR phase center (z_ϕ) and SAR backscatter (σ^0) along a profile on Kongsvegen glacier, Svalbard, at different frequency bands. We use L-, S- and C-band GPR profiles to calculate z_ϕ and σ^0 is extracted along the GPR profiles from L-band (PALSAR) and C-band (ASAR) images.

The phase centers in the frequency bands S and C, z_ϕ^S and z_ϕ^C, align with the previous summer surface (PSS) in the glacier ice (GI) and increase in depth within the super-imposed ice (SI) towards the firn zone. The pattern is similar for z_ϕ^L, though it resides well below the PSS in the ablation area and lies generally three times deeper than z_ϕ^S and z_ϕ^C.

The L-band backscatter, σ_L^0, is weak over GI and SI and increases drastically by 10 dB at the transition to the firn zone. We observe stronger σ_C^0 in the GI and SI, but with a higher variability than σ_L^0. Values of σ_C^0 and σ_L^0 are both relatively high in the firn zone, but σ_C^0 lacks the drastic increase observed in σ_L^0.

We attribute the increase in σ^0 along with the increase in z_ϕ to a change in the scattering mechanism along the glacier. In the lower parts of the glacier surface scattering at the PSS dominates. Ice glands in the SI cause volume scattering in addition to the surface scattering at the PSS. We speculate that the volume scattering leads to the increase in z_ϕ, while σ^0 stays weak due to the specular reflection at the PSS. We do not observe the reflection of PSS in the firn zone, where alternating firn and ice layers are the source for volume scattering. Thus, more energy transmits into the firn and is scattered back from the firn-ice interfaces giving a high σ^0.

The striking difference in σ_L^0 between the firn zone and the lower zones allows us to estimate the extent of the entire firn zone of Kongsvegen. We classify σ^0 by a simple threshold combined with the glacier outlines from a glacier database. Our firn area extent of around 27.5 km^2 agrees well with previously reported values in the range 22-36 km^2.

2.4 Relevant presentations and posters

Radar Scattering Zones Across Dronning Maud Land, East Antarctica: Preliminary results and observations from the 2007/2008 NOR-U.S. IPY traverse, Karsten Müller, Mary Albert, Svein-Erik Hamran, and Jon-Ove Hagen, *IGS Radioglaciology Meeting, Madrid*, June 2008

Relation between GPR, SAR and accumulation rate in the dry-snow zone of East Antarctica, Karsten Müller, Svein-Erik Hamran, Jon-Ove Hagen, and Anna Sinisalo, *IGS Nordic Branch Meeting, Helsinki*, October 2008

An 860 km surface mass balance profile in East Antarctica derived by GPR, Karsten Müller, Helgard Anschütz, Anna Sinisalo, Svein-Erik Hamran, Jon-Ove Hagen, Joseph R. McConnell, and Daniel R. Pasteris, *IGS Science in IPY Meeting, Northumbria*, July 2009 (poster)

Surface mass balance along the Norwegian-U.S. scientific traverse across East Antarctica, Karsten Müller, Helgard Anschütz, Anna Sinisalo, Svein-Erik Hamran, Jon-Ove Hagen, Joseph R. McConnell, Daniel R. Pasteris, and Elisabeth Isaksson, *AGU Fall Meeting, San Francisco*, December 2009

Microwave penetration in polar, snow, firn, and ice, Karsten Müller, Svein-Erik Hamran, Anna Sinisalo, and Jon-Ove Hagen, *IPY Oslo Science conference, Oslo*, June 2010 (poster)

Beneath the surface of the Recovery Lakes, Anna Sinisalo, Karsten Müller, Kirsty Langley, Helgard Anschütz, Jack Kohler, Svein-Erik Hamran, Mats-Jørgen Øyan, Jon-Ove Hagen, Elisabeth Isaksson, Gudmund Melland, Joseph R. McConnell, and Thomas A. Neumann, *IPY Oslo Science conference, Oslo*, June 2010 (poster)

2.5 GPR processing package *processgpr*

A tremendous amount of GPR data were acquired during the Norwegian - U.S. IPY traverse using two custom made GPR systems, i.e. C-band and UWB. Both GPRs have their own data format, system settings, and processing needs. To efficiently handle and process these data we developed a custom made processing software package named *processgpr*. The Python (`www.python.org`) programming language was chosen due to its easy and rapid code development cycle, yet powerful numerical capabilities. The package contains three sub-packages, i.e the core package, the extension package, and the tools package. The software package can be downloaded from `processgpr.sourceforge.net`.

The core package gathers general data import and export functionality and GPR processing routines. Raw GPR data from both systems is stored in binary file and a position file containing GPS coordinates and recording times. The raw data are pre-processed to the state where a time-domain wavelet or envelope is available and unwanted sections are removed. Bandpass filtering, before the FFT conversion is optional. All data (signal samples, meta data, and GPS coordinates per trace) are then stored in a single hierarchal data format file version 5, short HDF5 (`www.hdfgroup.com`). Common processing steps thereafter are stacking, gain, and static or topographical corrections. Each processing step is documented in the Python code itself. The extension package contains methods specific for individual radars. Currently are the UWB and C-band radars and their modifications as well as the MalåGeoscientific format supported.

The main features in the tools package are the *traceViewer* and the *gprViewer*, allowing 1D and 2D data visualization, respectively. Methods for calculating the phase center and power penetration depth are also part of the tool package. Routines that handle horizon picking and GPS conversions are also available.

Chapter 3

Conclusions and outlook

In this thesis, we calculated the distance to the phase center (z_ϕ) in snow and ice at several sites in Antarctica and on Kongsvegen glacier on Svalbard. The phase center reveals the position of the most effective scatterers within the snowpack. To our knowledge, this is the first time that z_ϕ in snow and ice is measured by GPR.

We show that there exists a substantial elevation bias in InSAR derived topography over major parts of ice sheets and glaciers. In the dry firn of Antarctica the distance to z_ϕ from the snow surface exceeds 40 m at L-band frequencies. In coastal Antarctica and on the Arctic glacier, z_ϕ resides ≈10 m below the snow surface at L-band. For higher frequencies in the S- and C-bands, z_ϕ shrinks to a mean of ≈4 m. Thus, a substantial elevation bias in InSAR topography measurements over such areas exists. However, we found that z_ϕ aligns with the previous summer surface in the ablation zone of Kongsvegen. This implicates that InSAR topography is correct over pure glacier ice.

A change in the scattering mechanisms dominating SAR backscatter along a glacier allows us to map the extent of the glacier's firn area. The comparison of z_ϕ with SAR backscatter showed a change in the scattering mechanisms along Kongsvegen glacier, Svalbard. This shift from surface scattering in the lower part to volume scattering in the firn area of the glacier leads to an abrupt increase in L-band SAR backscatter.

Microwave penetration allows us to gain information from within the snow or ice in a non-destructive manner. We used the penetration of microwaves into snow and ice to study the surface mass balance (SMB) and its variability in a previously unmapped part of the East Antarctic Plateau. The results indicate either an increase in the accumulation rate in recent decades or an overestimation by the previous studies. The

200 year mean SMB found in our study area is up to 50% lower than estimated by remote sensing and modelling over a period shorter than 50 years.

The field campaigns conducted during this thesis produced a wealth of GPR data. Most unique here are the GPR profiles along the Norwegian-US traverse across East Antarctica. We suggest to extend the SMB study for the return route from South Pole to Troll using the higher quality data of the UWB radar. By interpolating the SMB values between the two traverse legs by SAR imagery as presented in the extension to Paper I we can obtain an SMB estimate covering major parts of the East Antarctic plateau. Similarly, we suggest to calculate z_ϕ along the traverse route to get a better understanding of its variation in Antarctica. We do find, on random tests made on the GPR data between the Recovery Lakes and Kohnen station, that z_ϕ varies between 35-46 m, as given in Paper II.

The studies on Kongsvegen should be applied to other glaciers to investigate if the change in the scattering mechanism occurs on other glaciers, too. Likewise, it would be interesting to see if the simple threshold classification using L-band SAR backscatter works on other glaciers.

Chapter 4

Paper I

An 860-km surface mass balance profile on the East Antarctic Plateau derived by GPR

Karsten Müller, Anna Sinisalo, Helgard Anschütz, Svein-Erik Hamran, Jon-Ove Hagen, Joseph R. McConnell, and Daniel R. Pasteris

Annals of Glaciology, 51(55), 1-8.

Abstract

Snow accumulation and its variability on the East Antarctic Plateau are poorly understood due to sparse and regionally confined measurements. We present a 5.3 GHz (C-band) ground penetrating radar (GPR) profile with a total length of 860 km recovered during the joint Norwegian - U.S. IPY traverse 2007/2008. Mean surface mass balance (SMB) over the last 200 years was derived from the GPR data by identifying the volcanic deposition of the Tambora eruption in 1815. It varies between 9.1 and 37.7 kg m^{-2} a^{-1} over the profile with a mean of 23.7 kg m^{-2} a^{-1} and a standard deviation of 4.7 kg m^{-2} a^{-1}. The 200-year SMB estimated is significantly lower than most of the SMB estimates over shorter time periods in this region. It can be partially explained by a SMB minimum in the vicinity of the ice divide. However, it is more likely that a recent increase in SMB observed by several studies is largely responsible for the observed discrepancy.

4.1 Introduction

Many studies have recently concentrated on the surface mass balance (SMB) (Arthern et al., 2006; Monaghan et al., 2006; Van De Berg et al., 2006; Vaughan et al., 1999) and mass changes (Davis et al., 2005; Zwally et al., 2005) of the Antarctic ice sheet to assess Antarctica's contribution to changes in global sea level. New techniques, such as radar altimetry have made it possible to study continent wide elevation changes with high accuracy. These changes are often related to changes in precipitation on the East Antarctic Plateau (EAP) (Davis et al., 2005; Zwally et al., 2005). However, these techniques cover only short time periods, and it is important to obtain ground truth over longer time periods to understand how observed changes relate to the past.

To date, there have been very few in-situ measurements of SMB available from the interior of the EAP, and the present SMB estimates are based mainly on remote sensing (e.g. Arthern et al., 2006) or numerical modeling (e.g. Monaghan et al., 2006; Van De Berg et al., 2006) calibrated by very sparse in-situ measurements for the interior of the continent. There are also indications that there is a non-negligible number of zero accumulation sites, so called glazed areas, in the interior of the EAP that are often not taken into account by mass balance estimates, but can change their value significantly (Scambos et al., 2008; Frezzotti et al., 2002). It is clear that more accumulation data are required to study the spatial and temporal variability of SMB, and to improve the spatial resolution and accuracy of large scale accumulation studies.

The SMB is the aggregate of many processes, such as precipitation from clouds and clear skies, the formation of hoarfrost at the surface and within the snowpack, sublimation, melting and runoff, wind scouring, and drift deposition (Eisen and Others, 2008). Snow accumulation can be derived using various methods (e.g. Eisen and Others, 2008). Snow pit, firn and ice core studies provide valuable information about mean SMB for a certain point location (Anschütz et al., 2009; Isaksson et al., 1996; Takahashi et al., 1994). These point measurements can be spatially extended by ground penetrating radar (GPR). SMB is proportional to the reflector depth within the firn pack as variations in vertical strain rates can be neglected in the top tens of meters of the ice sheet (Nye, 1963). Previously, GPR has been successfully used to follow isochronous firn layers providing detailed information about the SMB variability across Antarctica (Arcone et al., 2005a; Spikes et al., 2004; Richardson-Näslund, 2004; Rotschky et al.,

2004; Fujita et al., 1999) although large regions of the EAP still remain uncovered.

We show SMB derived by GPR data collected during the first leg of the Norwegian - U.S. Scientific Traverse of East Antarctica (http://traverse.npolar.no/) in austral summer 2007/2008. This joint project is part of the larger Trans-Antarctic Scientific Traverses Expeditions - Ice Divide of East Antarctica (TASTE-IDEA) and the International Partners in Ice Coring Sciences (IPICS) (Goldman, 2008).

4.2 Study site

Our 860 km long profile goes across one of the least known parts of East Antarctica (Fig. 4.1). The profile is following one of the main ice divides on the inland side of it, 100-200 m below its crest passing five firn cores at sites NUS07-2, -3, -4, -5, and -6 drilled during the traverse (Fig. 4.1). The study area extents from 76.1° to 81.4° South and 22.5° to 49.4° East with increasing elevation from 3580 m to 3680 m along the profile (Fig. 4.2a). The annual mean temperature is about -50 °C (Comiso, 2000), and the annual mean wind speed remains usually below 6 m s^{-1} (Van Lipzig et al., 2004) in the study area.

Previous measurements of SMB have been made as point measurements from snow pits and firn cores in the surrounding of the ice divide and the near plateau region (Takahashi et al., 1994; Endo and Fujiwara, 1973; Picciotto et al., 1971). The JARE South Pole traverse 1968-69 crossed our profile at Plateau Station, and measured a SMB about 30 kg m^{-2} a^{-1} from a snow pit there (Endo and Fujiwara, 1973). Picciotto et al. (1971) measured a SMB of 27 kg m^{-2} a^{-1} at Plateau Station and 31kg m^{-2} a^{-1} for Pole of Inaccessibility for the time period 1955-65. Takahashi et al. (1994) measured SMB by gross β activity of 35 and 33 kg m^{-2} a^{-1} at two sites on the eastern flank of the ice divide at elevations of 3648 and 3761 m, respectively. Analysis of NUS07-3, -4, and -6 indicate SMB of less than 22 kg m^{-2} a^{-1} over the last 200 years in the study area (Anschütz et al., 2009).

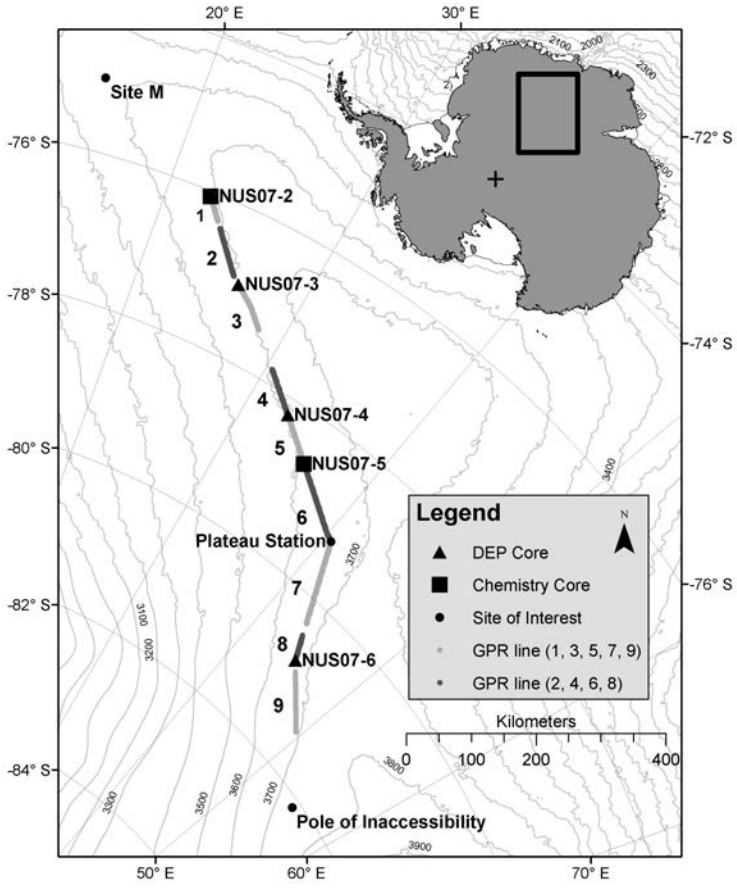

Fig. 4.1: *Map of the study area. GPR sections 1-9 are shown as alternating light and dark grey lines. Firn core sites used as GPR tie points are indicated as black triangles (DEP) and black squares (chemistry). Topography is shown as 100 m contour lines taken from the RadarSat Antarctic Mapping Project Digital Elevation Model (Jezek and Team, 2002).*

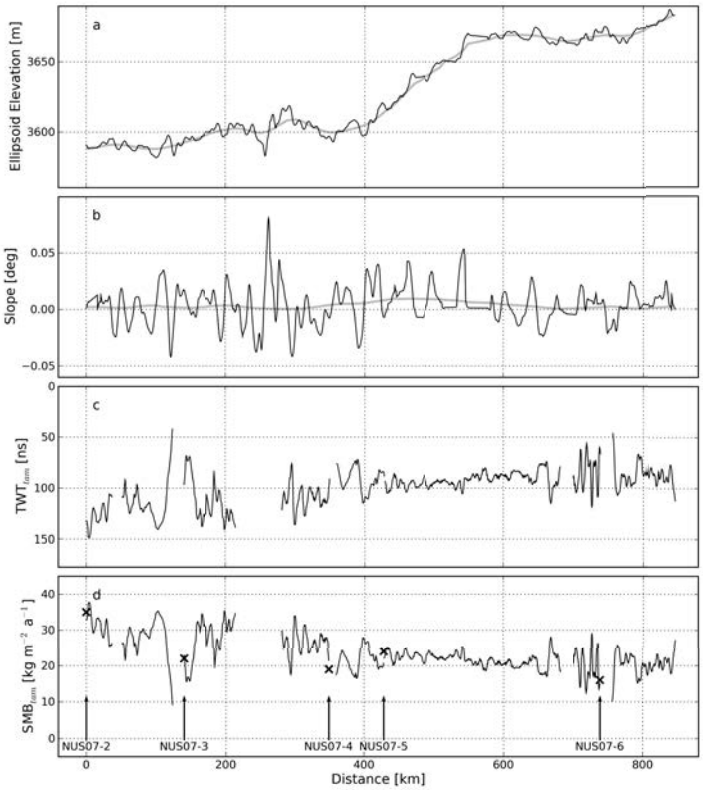

Fig. 4.2: *a) Elevations above WGS-84 ellipsoid for the snow surface along the GPR profile (black line) and the large scale topography smoothed over 100 km (grey line). b) Slope in degrees for 10 km (black line) and 100 km (grey line) intervals of the surface elevation. c) The depth to the Tambora deposition expressed as TWT of the GPR signal. d) SMB_{tam} calculated applying Equation 4.3.3 and location and SMB estimates (crosses) of the tie points.*

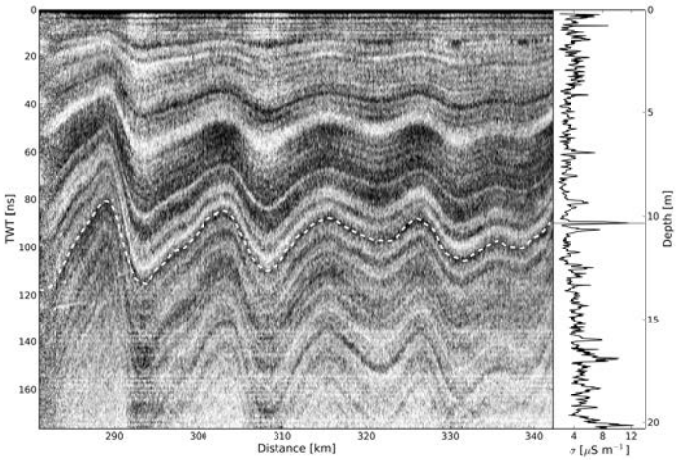

Fig. 4.3: *GPR section 4 (left) with the conductivity-depth distribution from firn core NUS07-4 (right) drilled at the end of section 4. The conductivity curve shows a clear double peak at the depth of Tambora, and it was used as a tie for the GPR data. The picked Tambora layer is indicated as a white dashed line. The depth axis to the right is calculated for a velocity of 0.23 m ns^{-1}. The distance axis is with regrad to the total profile length as in Fig. 4.2.*

4.3 Methods

4.3.1 Ground penetrating radar

We used a frequency-modulated continuous-wave (FMCW) radar, which is an updated version of the radar described in Hamran and Langley (2006). The system has a center frequency of 5.3 GHz and sweeps over a bandwidth of 1 GHz. The unambiguous range in air is 67.4 m with 451 samples in the frequency domain. Its two quad ridged horn antennae were separated by 10 cm and are treated as monostatic. They were suspended 65 cm above the snow surface extending from the side of a Berco TL6 tracked vehicle. Traces were collected every 0.2 s, which corresponds to a trace interval of approximately 0.4 m at an average driving speed of 2 m s^{-1}.

Data are recorded in the frequency domain and transferred to time domain by Fast Fourier Transform (FFT) after Hamming window filtering. Each trace contains 1024 samples with a time increment of 0.219 ns. The effective time window (measured from the snow surface reflection) is 177 ns corresponding to a penetration depth of about

20 m in dry polar firn (Fig. 4.3). The nominal vertical resolution in air is 15 cm and 11 cm in a firn pack with rel. permittivity of 1.8, corresponding to a density of 400 kg m^{-3} (Kovacs et al., 1995). GPR traces were collected at equal time intervals of 0.2 s. Signal to noise ratio was improved by stacking traces over 10 m intervals determined by the GPS coordinates, which on average correponds to a 25-fold trace stack at a driving speed of 2 m s^{-1}. We converted amplitude values to weighted backscatter in dB as described in Langley et al. (2007) to compensate for spreading losses and increase display quality.

4.3.2 Global positioning system

Global positioning system (GPS) elevation data were recorded together with the GPR data. A Garmin 60CSx hand-held unit with external antenna was directly connected to the GPR system and recorded the latitude, longitude and GPS time every two seconds. In addition a Trimble geodetic GPS system collected positioning data including elevation every second. The Trimble raw data format was processed using Terratec's TerraPos software, which allows high precision for kinematic GPS measurements. Decimeter precision in x and y and sub-meter precision in elevation is achieved by employing precise satellite orbits and satellite clock corrections coupled with state-of-the-art error modeling without a need for a reference station (Zumberge et al., 1997). GPS elevations from the Trimble data were aligned with the hand-held units using the GPS time stamps. The offset between the external Garmin and Trimble antenna was 0.5 m. The elevations above the WGS-84 ellipsoid for the snow surface are shown as a black line in Fig. 4.2a. The elevation data was smoothed over 100 km to represent the large scale topography. Slopes over 10 km and 100 km were calculated to represent changes in the small scale and large scale topography, respectively (Fig. 4.2b).

4.3.3 Firn cores

Five firn cores labeled NUS07-2 to -6 along the GPR profile served as calibration points for the GPR data (Fig. 4.1 and Table 4.1). A broad range of chemical species and elements including total sulfur were measured in firn cores NUS07-2 and -5 using a continuous melter system coupled to two High Resolution Inductively Coupled Plasma Mass Spectrometers (HR-ICP-MS) (McConnell et al., 2002; McConnell and Edwards,

Table 4.1: *Firn cores used in this study. The distance (x) denotes the distance along the GPR profile. Negative values give the shortest distance to NUS07-2, the start of the profile. The depth and two-way traveltime to the Tambora deposition are denoted by d_{tam} and TWT_{tam}, respectively.*

Core	Position	x [km]	d_{tam} [m]	TWT_{tam} [ns]	Method	Reference
Site M	75.00°S 15.00°E	-240	18.84	163.8	Chemistry, DEP	Hofstede et al. (2004)
NUS07-2	76.07°S 22.46°E	0	15.2	132.2	Chemistry	this study
NUS07-3	77.00°S 26.05°E	140	10.89	94.7	DEP	Anschütz et al. (2009)
NUS07-4	78.22°S 32.85°E	350	10.33	89.8	DEP	Anschütz et al. (2009)
NUS07-5	78.65°S 35.64°E	428	11.60	100.9	Chemistry	this study
NUS07-6	80.78°S 44.84°E	739	8.98	78.1	DEP	Anschütz et al. (2009)

2008). While the distinctive double peaks associated with fallout from the Tambora 1815/unknown 1809 depositions were readily identified in each core, we confirmed the dating using comparisons to similar measurements in cores from high snow accumulation regions. Tambora refers to a historically known eruption of the Tambora volcano in 1815, which is assumed to be deposited in Antarctica in 1816 (Traufetter et al., 2004). In addition, cores NUS07-3, -4, and -6 were previously dated by dielectric profiling (DEP) (Anschütz et al., 2009). The Tambora deposition was identified as a characteristic double peak in the normalized conductivity.

4.3.4 Surface mass balance

Mean SMB along the GPR profile was derived by following widely used processing steps summarized by Eisen and Others (2008): i) track isochrones, ii) make a time-depth conversion, iii) make an age estimation from available cores, and iv) calculate SMB from cumulative mass. We started by making a depth-time conversion for the Tambora layer identified in the firn cores along the profile in order to tie in the GPR profile (Table 4.1). The DEP derived permittivity values were converted to interval velocities which were then averaged to the known depth of Tambora for each of the DEP sites individually. The mean velocities to the depth of Tambora were 0.23 m ns^{-1} (NUS07-3), 0.24 m ns^{-1} (NUS07-4) and 0.23 m ns^{-1} (NUS07-6). These velocities were used to calculate the two-way traveltime (TWT) to Tambora at DEP core sites (Table 4.1). A microwave velocity of 0.23 m ns^{-1} was assumed when calculating the TWT to Tambora at core sites NUS07-2 and -5, and for the general depth-time conversion of the GPR data. Thus, depth d of the picked layer in the GPR data could be calculated as $d = TWT \div 2 \cdot 0.23$ m ns^{-1}. Fig. 4.3 shows GPR section 4 as an example and the tie to Tambora identified in core NUS07-4. A reflector or a pattern of reflectors were followed in the GPR data starting from the calculated depth at the core site.

We need to estimate the mass accumulated over time in order to convert the picked depth to SMB. Measured bulk densities of the firn core pieces (ρ_i) from all five cores were converted to mean bulk densities ($\bar{\rho}_i$) over depth by

$$\bar{\rho}_i = \frac{\sum_i \rho_i \cdot l_{int,i}}{\sum_i l_{int,i}} \tag{4.3.1}$$

where i denotes the depth interval and $l_{int,i}$ is the length of the core piece at that

interval.

The density distribution with depth for all cores is similar (see Fig. 4.4) with a standard deviation of 30.4 kg m^{-3} from mean $\bar{\rho}$ for all cores. We therefore assume a laterally homogeneous firn pack represented by a second-order polynomial (Equation 4.3.2) fitted to these densities in the depth range of 0 to 26 m (Fig. 4.4).

$$\bar{\rho}(d) = -0.0597392295 \cdot d^2 + 6.31246760e \cdot d + 330.422375 \tag{4.3.2}$$

Correlation coefficients between measured and calculated densities are higher than 0.95. We calculate a mean SMB along the GPR transect over the last 200 years by using Equation 4.3.3.

$$SMB_{tam}(d) = \frac{d \cdot \bar{\rho}(d)}{a} \tag{4.3.3}$$

where SMB_{tam} is the mean SMB since Tambora in kg m^{-2} a^{-1}, d is the depth to the reflecting horizon calculated from the GPR TWT, and a equals the 191 years time span between the Tambora deposition in 1816 and collection of the firn cores and GPR data in 2007/2008.

The GPR profile was divided into nine sections with regard to data gaps. The sections were numbered from North to South from 1 to 9 as indicated in Fig. 4.1. Gaps in the GPR profile result from very poor data quality due to temperature sensitivity of the system or glazed areas previously identified using satellite imagery (Scambos et al., 2008; Frezzotti et al., 2002) around km 123 and km 270. Over these discontinuities it was not possible to follow the reflector. However, five firn cores allowed us to tie in most GPR sections directly, and the gaps to GPR sections where no tie point was available were overcome by layer pattern comparison as the example in Fig. 4.5 shows. All gaps along the GPR profile account for a total length of 133 km with the longest gap (61 km) between sections 3 and 4.

The total length of the accumulation profile derived from the GPR data was limited by two factors. Firstly, the depth to the Tambora layer is almost 19 m at Site M (Hofstede et al., 2004) north of the start of the profile (Fig. 4.1), which is close to the maximum penetration depth of our GPR. The signal to noise ratio does not allow a clear identification of a single reflector at that depth anymore. Secondly, the data quality decreases due to temperature sensitivity of the system at the end of section 9

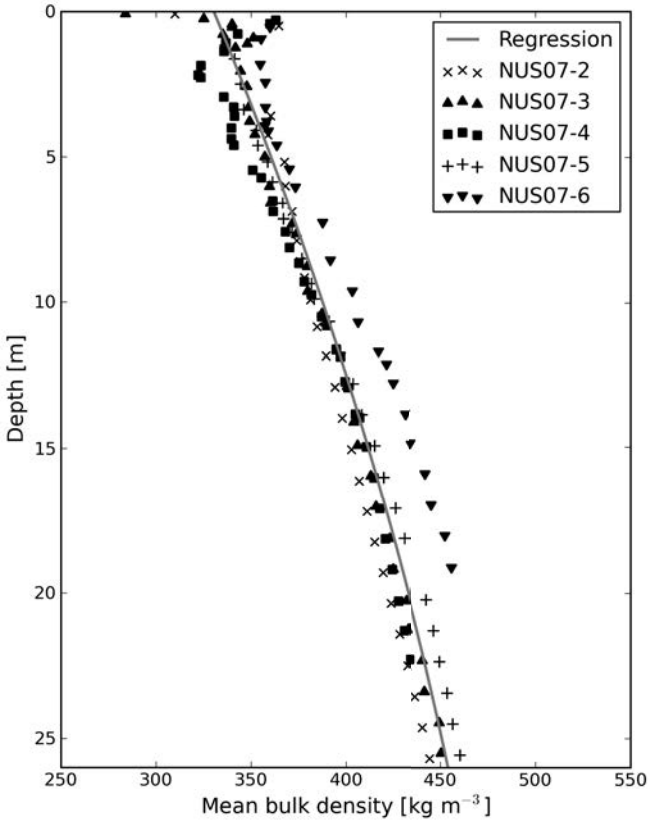

Fig. 4.4: *Mean measured bulk density to depth values from firn cores NUS07-2, -3, -4, -5, and -6. The density depth relation for the SMB calculation is a second-order polynomial fit (Equation 4.3.2) to these values over the shown depth range (grey line).*

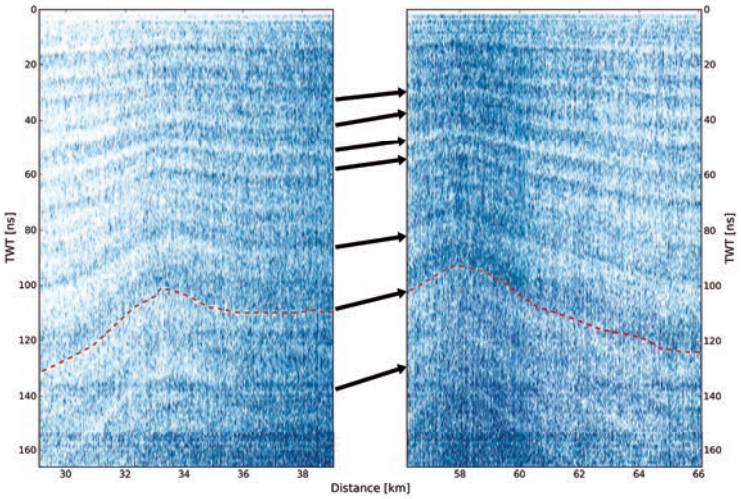

Fig. 4.5: *The last 10 km of GPR section 1 (left) and the first 10 km of section 2 (right) showing how it was possible to track Tambora over a gap in GPR data. Arrows indicate patterns of layers which are identified on both sides of the gap. The picked Tambora layer is indicated by a white dashed line. The distance axis is with regrad to the total profile length as in Fig. 4.2.*

south of NUS07-6, which prohibited tracing the Tambora layer farther South.

4.4 Results and discussion

The Tambora layer identified in the firn cores NUS07-2 to -6 was followed over the 860 km long GPR profile shown in Fig. 4.1. Its depth derived from the GPR TWT (Fig. 4.2c) varies between 4.8 m and 17.1 m decreasing southwards. Applying equation 4.3.3 gives SMB_{tam} between 9.1 and 37.7 kg m^{-2} a^{-1} along the profile with a mean of 23.7 kg m^{-2} a^{-1} and a standard deviation of 4.7 kg m^{-2} a^{-1} over the period from 1816 to 2007/2008 (Fig. 4.2d). The profile shows that five firn cores used to calibrate the GPR data represent minima in SMB along the profile. The trend along our profile shows a decrease in SMB_{tam} by 1.3 kg m^{-2} a^{-1} per 100 km from North to South, correlating with increasing elevation and continentality as previously observed on EAP (Anschütz et al., 2009; Takahashi et al., 1994).

The characteristic of SMB_{tam} variability changes along the profile. On the first 410

km and the last part from 660 km onwards SMB_{tam} has higher variability compared to the part inbetween. SMB_{tam} varies between 38 and 16 kg m^{-2} a^{-1} over the first 410 km of the profile, where changes of up to 17 kg m^{-2} a^{-1} over a distance of 4 km occur. Elevation increases gently over this part of the profile, but small surface undulations of a few meters on a 10-20 km scale characterize the topography. Slopes over 10 km vary between 0.04° and -0.04° (Fig. 4.2b). King et al. (2004) demonstrated that very small topographic variations, particularly on small spatial scales, can have a disproportional large impact on snow accumulation. Since precipitation will not vary on such a local scale, we conclude that changes in wind vectors due to these undulations are the reason for the high variability. The flat large scale topography (grey line in Fig. 4.2a,b) does not allow high katabatic wind speeds and therefore snow will not travel far, but only be redistributed locally. Over the last 200 km of the profile topographical features are similar to those on the first 410 km and the variability in SMB_{tam} is the same as for the first 410 km. The mean SMB_{tam} of 20 kg m^{-2} a^{-1}, though is slightly lower due to the increased elevation and continentality.

Between km 410 and km 660 the elevation rises by 70 m showing the steepest large scale topographical change along the profile. Here SMB_{tam} is fairly constant around 21 kg m^{-2} a^{-1}, varying only by ± 3 kg m^{-2} a^{-1} (14%). Changes in SMB_{tam} over 5 km are at a maximum 4 kg m^{-2} a^{-1}. The steeper large scale slope allows higher wind speeds that move mass downslope. Local redistribution on the 10-20 km scale is therefore smaller and the SMB_{tam} down-slope will be higher as can be observed in our profile (Fig. 4.2d).

No overall correlation between small scale surface topography and SMB_{tam} could be found although higher accumulation aligns in some parts with troughs and gentle slopes (e.g. km 395) and lower accumulation with bumps and steeper slope (e.g. km 185) as also observed by Takahashi et al. (1994) on the scale of 10-30 km on EAP. The arbitrary orientation of the profile with regard to the largest slopes and/or largest wind vector may explain why no relationship between SMB and slope as for the West Antarctic Ice Sheet (Arcone et al., 2005b) was found. It should be noted, however, that the glazed areas at km 123 and km 270 align with the largest small scale slopes along the profile (Fig. 4.2b). Our data do not allow us to determine if the SMB in these areas is only very small, zero or even negative.

Generally, our SMB values are lower than found in this region earlier. However, the previous direct SMB measurements cover more recent, much shorter time periods after 1950, from a few years up to a few decades, and their spatial representativity remain unknown.

Our results show that the 200-year mean SMB along our profile is up to 70% lower than estimated in the continent-wide SMB studies for the last 50 years by Arthern et al. (2006), Monaghan et al. (2006), and Van De Berg et al. (2006) although the regional trend showing a decrease from the start of the profile to about km 450 and then a fairly constant SMB is represented by all studies. Part of the discrepancy can be explained by an accumulation and density minimum in the vicinity of the crest of the ice divide where our profile is located (Endo and Fujiwara, 1973). The grid resolution of the continent-wide compilations is equal to or larger than 55 km. The map values will therefore represent the average over $3{\cdot}10^3$-$10{\cdot}10^3$ km^2. As there are no in-situ SMB data perpendicular to our profile, it is impossible to estimate how well our GPR line represents the areal average. On the other hand, the large scale maps are guided by previously very sparse in-situ measurements in this area and the spatial density of those will affect their accuracy.

It is more likely, however that a recent increase of SMB observed on EAP (e.g. Davis et al., 2005; Zwally et al., 2005) can explain the differences between previous SMB estimates and our data averaged over the last 200 years. The increase is also indicated by firn and ice core studies at both ends of our GPR profile (Hofstede et al., 2004; Mosley-Thompson et al., 1999), and in several other places on EAP during the last 50 years (Frezzotti and Others, 2005; Stenni and Others, 2002; Oerter et al., 1999). For example, Mosley-Thompson et al. (1999) report an SMB increase of 30% at South Pole since the 1960s. The large scale studies have calibrated their SMB maps using these data, which may also partially explain the large differences between our 200-year mean SMB and their SMB values for the last 50 years.

4.4.1 Error estimates

Uncertainties in the GPR derived layer depth and conversion to SMB_{tam} originate from four main sources: i) unknown density distribution between firn cores, ii) layer picking, iii) digitization, and iv) uncertainty in dating. Error estimates in SMB_{tam} are

with regard to the time period 1816 to 2007/2008. The errors increase with depth due to the compaction of the firn pack. Following maximum errors are therefore always given for the deepest layer found at 17.1 m.

i) The largest error is assumed to result from firn density variations over depth and in between the core sites. Maximum deviation from the mean density of all cores at a certain depth interval is 30.4 kg m^{-3}. This was assumed to be the standard error in density since only one measurement was taken at each location. The largest error in SMB_{tam} due to the maximum standard error in density (δ_ρ) is calculated by differentiating Equation 4.3.3 with respect to ρ and multiplication by 30.4 kg m^{-3} giving 2.7 kg m^{-2} a^{-1}. ii) The high frequency of the GPR used, results in strong diffuse scattering rather than specular reflections from interfaces of different dielectric properties. Therefore horizons in the GPR profile appear very broad and picking a single layer is difficult. We estimate the uncertainty to be ± 2 ns. That corresponds to an uncertainty in depth of 0.46 m assuming a microwave velocity of 0.23 m ns^{-1}. The maximum error in SMB_{tam} due to the uncertainty in picking (δ_p) is calculated by differentiating Equation 4.3.3 with respect to d (taking into account that ρ is also a function of d) and multiplying it by 0.46 m, which gives 1.2 kg m^{-2} a^{-1}. iii) Inaccurate isochrone depth results also from the digitization of the recorded radar signal. The sampling interval in time is 0.219 ns, which corresponds to an uncertainty in depth of about 0.025 m. Calculating the error in SMB_{tam} from digitization (δ_d) as in (ii) gives a negligible value of 0.065 kg m^{-2} a^{-1}. iv) GPR reflections do not represent annual firn layers since the annual layer thickness is less than the GPR could resolve. For example at site NUS07-3 the Tambora deposition was identified at a depth of 10.9 m. That would mean an average annual layer thickness of 0.06 m, where compression will lead to tighter layers with depth. Having a nominal resolution of 0.11 m in a firn pack of 400 kg m^{-3} density, our GPR detects an integrated signal over 2 annual firn layers at best. Broadening introduced by the Hamming window filter and diffuse scattering from interfaces though will result in even lower resolution in practice. The absolute errors for SMB_{tam} in the cores NUS07-3, -4, and -6 lie in the range of 0.3 to 0.5 kg m^{-2} a^{-1}. Anschütz et al. (2009) give an error of 2.3% in dating the firn cores for the period 1816-2007/2008. We therefore assume an error in dating of 4.3 years. Equation 4.3.3 is differentiated with respect to a and multiplied by 4.3 years giving the maximum error

in SMB_{tam} with regard to age (δ_a) of 1.1 kg m^{-2} a^{-1}. The combined maximum error from sources i) - iv) is calculated as follows:

$$\delta_{SMB} = \sqrt{\delta_\rho^2 + \delta_p^2 + \delta_d^2 + \delta_a^2} \tag{4.4.1}$$

The estimated maximum, cumulative error is 3.1 kg m^{-2} a^{-1} found for the deepest layers at 17.1 m decreasing for more shallow parts. It should also be noted that very low or zero accumulation sites (glazed areas) were excluded from the study since it was not possible to trace layers over them. Thus, the mean SMB_{tam} along the profile may therefore be slightly lower than the value of 23.7 kg m^{-2} a^{-1}.

4.5 Conclusions

We show a continuous SMB profile in a previously uncovered area of EAP where sparse in-situ measurements have been available. We used a high frequency FMCW GPR to interpolate SMB measured by DEP and sulfur concentration from firn cores. The mean SMB over the last 200 years along our 860 km long profile is 23.7 kg m^{-2} a^{-1}, with an assumed maximum error of 3.1 kg m^{-2} a^{-1}. Increasing elevation and continentality lead to a decrease in SMB by about 1.3 kg m^{-2} a^{-1} per 100 km towards South along the profile. SMB ranges from 9.1 to 37.7 kg m^{-2} a^{-1} along the whole profile.

The 200-year SMB along our profile is significantly lower than most of the SMB estimates over shorter time periods in this region. It can be partially explained by a SMB minimum in the vicinity of the ice divide. However, it is more likely that a recent increase in SMB observed by several studies (Davis et al., 2005; Frezzotti and Others, 2005; Zwally et al., 2005; Hofstede et al., 2004; Stenni and Others, 2002; Mosley-Thompson et al., 1999; Oerter et al., 1999) is largely responsible for the observed discrepancy.

This is the first time that small scale variability of SMB is defined for this region. SMB has a standard deviation of 4.7 kg m^{-2} a^{-1} corresponding to an average variation around the mean of about 20%. The variations are connected to the surface topography with undulations of 10-20 km wave length over the flat parts. Variation can be as high as 17 kg m^{-2} a^{-1} over 4 km, but are generally lower than 10 kg m^{-2} a^{-1} over that distance. On the slope from km 410 to km 660 the variability decreases. This is assumed to be due to a large scale slope allowing higher wind speeds that are capable

of moving snow to distant areas instead of redistributing it locally. The results show that the SMB point measurements by Anschütz et al. (2009) used as tie points for our GPR data were located on the low accumulation sites along the profile giving up to 33% smaller SMB than the profile mean.

4.6 Acknowledgments

The paper is a contribution to the Norwegian-US Antarctic IPY traverse with funding from the Norwegian Research Council, Norwegian Polar Institute and National Science Foundation. We thank G. Melland and S. Trondstad from NPI for the processing of the GPS data. Special thanks go to the members of the traverse team for making this work possible. We thank Kenny Matsuoka and two anonymous reviewers for their valuable input and comments.

References

Anschütz, H., Müller, K., Isaksson, E., McConnell, J. R., Fischer, H., Miller, H., Albert, M. R., and Winther, J.-G. (2009). Revisiting sites of the South Pole Queen Maud Land Traverses in East Antarctica: Accumulation data from shallow firn cores. *J. Geophys. Res.*, 114(D24):D24106—-.

Arcone, S. A., Spikes, V. B., and Hamilton, G. S. (2005a). Phase structure of radar stratigraphic horizons within Antarctic firn. *Annals of Glaciology*, 41:10–16.

Arcone, S. A., Spikes, V. B., and Hamilton, G. S. (2005b). Stratigraphic variation within polar firn caused by differential accumulation and ice flow: interpretation of a 400 MHz short-pulse radar profile from West Antarctica. *Journal of Glaciology*, 51:407–422.

Arthern, R. J., Winebrenner, D. P., and Vaughan, D. G. (2006). Antarctic snow accumulation mapped using polarization of 4.3-cm wavelength microwave emission. *Journal of Geophysical Research*, 111, D0610.

Comiso, J. C. (2000). Variability and trends in Antarctic surface temperatures from in situ and satellite infrared measurements. *Journal of Climate*, 13:1674–1696.

Davis, C. H., Li, Y., McConnell, J. R., Frey, M. M., and Hanna, E. (2005). Snowfall-driven growth in East Antarctic Ice Sheet mitigates recent sea-level rise. *Science*, 308(1898).

Eisen, O. and Others, . (2008). Ground-based measurements of spatial and temporal variability of snow accumulation in East Antarctica. *Reviews of Gephysics*, 46, RG2001.

Endo, Y. and Fujiwara, K. (1973). Characteristics of the Snow Cover in East Antarctica along the Route of the JARE South Pole Traverse and Factors Controlling Such Characteristics. *JARE scientific reports. Ser. C, Earth sciences*, 7:1–38.

Frezzotti, M., Gandolfi, S., La Marca, F., and Urbini, S. (2002). Snow dunes and glazed surfaces in Antarctica: new field and remote-sensing data. *Annals of Glaciology*, 34:81–88(8).

Frezzotti, M. and Others, . (2005). Spatial and temporal variability of snow accumulation in East Antarctica from traverse data. *Journal of Glaciology*, 51:113–124.

Fujita, S., Maeno, H., Uratsuka, S., Furukawa, T., Mae, S., Fujii, Y., and Watanabe, O. (1999). Nature of radio echo layering in the Antarctic Ice Sheet detected by a two-frequency experiment. *Journal of Geophysical Research*, 104(B6):13,01313,024.

Goldman, H. V. (2008). From the editor: halfway through the IPY - halfway for an Antarctic traverse. *Polar Research*, 27:1–6.

Hamran, S.-E. and Langley, K. (2006). C-band Polarimetric GPR. In *11th International Conference on Ground Penetrating Radar*.

Hofstede, C. M., van de Wal, R. S. W., Kaspers, K. A., van den Broeke, M. R., Karlöf, L., Winther, J. G., Isaksson, E., Lappegard, G., Mulvaney, R., Oerter, H., and Wilhelms, F. (2004). Firn accumulation records for the past 1000 years on the basis of dielectric profiling of six firn cores from Dronning Maud Land, Antarctica. *Journal of Glaciology*, 50(169):279291.

Isaksson, E., Karlen, W., Gundestrup, N., Mayewski, P., Whitlow, S., and Twickler, M. (1996). A century of accumulation and temperature changes in Dronning Maud Land, Antarctica. *Journal of Geophysical Research*, 101(D3):70857094.

Jezek, K. C. and Team, R. P. (2002). RAMP AMM-1 SAR Image Mosaic of Antarctica. Fairbanks, AK: Alaska SAR Facility, in association with the National Snow and Ice Data Center.

King, J. C., Anderson, P. S., Vaughan, D. G., Mann, G. W., Mobbs, S. D., and Vosper, S. B. (2004). Wind-borne redistribution of snow across an Antarctic ice rise. *Journal of Geophysical Research*, 109(10.1029).

Kovacs, A., Gow, A. J., and Morey, R. M. (1995). The in-situ dielectric constant of polar firn revisited. *Cold Regions Science and Technology*, 23(3):245–256.

Langley, K., Hamran, S.-E., Hø gda, K.-A., Storvold, R., Brandt, O., Hagen, J.-O., and Kohler, J. (2007). Use of C-Band Ground Penetrating Radar to Determine Backscatter Sources Within Glaciers. *Geoscience and Remote Sensing, IEEE Transactions on*, 45(5).

McConnell, J. R. and Edwards, R. (2008). Coal burning leaves toxic heavy metal legacy in the Arctic. *Proceedings of the National Academy of Sciences*, 105(34):12140.

McConnell, J. R., Lamorey, G. W., Lambert, S. W., and Taylor, K. C. (2002). Continuous ice-core chemical analyses using inductively coupled plasma mass spectrometry. *Environ. Sci. Technol*, 36(1):7–11.

Monaghan, A. J., Bromwich, D. H., Fogt, R. L., Goodwin, I., and Dixon, D. A. (2006). Insignificant Change in Antarctic Snowfall Since the Internatioanl Geophysical Year. *Science*, 313(827).

Mosley-Thompson, E., Paskievitch, J., Gow, M., and Thompson, L. (1999). Late 20th century increase in South Pole snow accumulation. *Journal of Geophysical Research*, 104(D4):38773886.

Nye, J. F. (1963). Correction factor for accumulation measured by the thickness of the annual layers in an ice sheet. *Journal of Glaciology*, 4(36):785–788.

Oerter, H., Graf, W., Wilhelms, F., Minikin, A., and Miller, H. (1999). Accumulation studies on Amundsenisen, Dronning Maud Land, by means of tritium, dielectric profiling and stable-isotope measurements: first results from the 199596 and 199697 field seasons. *Annals of Glaciology*, 29:1–9.

Picciotto, E., Grozaz, G., and de Breuck, W. (1971). Accumulation on the South Pole Queen Maud Land Traverse, 1964-1968. Antarctic Snow and Ice Studies II. *Antarc. Res. Ser.*, 16:257–315.

Richardson-Näslund, C. (2004). Spatial characteristics of snow accumulation in Dronning Maud Land, Antarctica. *Global and Planetary Change*, 42(1-4):31–43.

Rotschky, G., Eisen, O., Wilhelms, F., Nixdorf, U., and Oerter, H. (2004). Spatial distribution of surface mass balance on Amundsenisen plateau, Antarctica, derived from ice-penetrating radar studies. *Annals of Glaciology*, 39:265–270.

Scambos, T., Haran, T., Frezotti, M., Jezek, K., Long, D., and K., F. (2008). Mapping East Antarctic wind glaze extent at high resolution from space: implications for East Antarctic ice mass balance. *Geophysical Research Abstracts*, 10, EGU200:SRef–ID: 1607–7962/gra/EGU2008–A–10755, EGU Genera.

Spikes, V. B., Hamilton, G. S., Arcone, S. A., Kaspari, S., and Mayewski, P. A. (2004). Variability in accumulation rates from GPR profiling on the West Antarctic plateau. *Annals of Glaciology*, 39:238–244.

Stenni, B. and Others, . (2002). Eight centuries of volcanic signal and climate change at Talos Dome (East Antarctica). *Journal of Geophysical Research*, 107(D9), 4.

Takahashi, S., Ageta, Y., Fujii, Y., and Watanabe, O. (1994). Surface mass balance in east Dronning Maud Land, Antarctica, observed by Japanese Antarctic Research Expeditions. *Annals of Glaciology*, 20:242.

Traufetter, F., Oerter, H., Fischer, H., Weller, R., and Miller, H. (2004). Spatio-temporal variability in volcanic sulphate deposition over the past 2 kyr in snow pits and firn cores from Amundsenisen, Antarctica. *Journal of Glaciology*, 50:137–146.

Van De Berg, W. J., den Broeke, M. R., Reijmer, C. H., and Van Meijgaard, E. (2006). Reassessment of the Antarctic surface mass balance using calibrated output of a regional atmospheric climate model. *Journal of Geophysical Research*, 111(D11104).

Van Lipzig, N. P. M., Turner, J., Colwell, S. R., and den Broeke, M. R. (2004). The near-surface wind field over the Antarctic continent. *International Journal of Climatology*, 24:1973–1982.

Vaughan, D. G., Bamber, J. L., Giovinetto, M., Russell, J., and Cooper, A. P. R. (1999). Reassessment of net surface mass balance in Antarctica. *Journal of climate*, 12(4):933.

Zumberge, J. F., Heflin, M. B., Jefferson, D. C., Watkins, M. M., and Webb, F. H. (1997). Precise point positioning for the efficient and robust analysis of GPS data from large networks. *Journal of Geophysical Research*, 102(B3).

Zwally, H. J., Giovinetto, M. B., Li, J., Cornejo, H. G., Beckley, M. A., Brenner, A. C., Saba, J. L., and Yi, D. (2005). Mass changes of the {G}reenland and {A}ntarctic ice sheets and shelves and contributions to sea-level rise: 1992-2002. *Journal of Glaciology*, 51(19):509–527.

Chapter 5

Extension to Paper I

5.1 Introduction

Recently, many studies have concentrated on the large scale SMB of the Antarctic continent (Arthern et al., 2006; Monaghan et al., 2006; Van De Berg et al., 2006; Vaughan et al., 1999) as it can play a major role in global sea level rise in a warming climate. To date, there have been very few measurements of SMB available from the interior of the East Antarctic plateau (EAP), and the present SMB estimates are based mainly on remote sensing (Arthern et al., 2006) or numerical modeling (Van De Berg et al., 2006) calibrated with very sparse ground truth data. There are also indications that the variability of the SMB in the interior of EAP can change the mass balance estimates significantly (Scambos et al., 2008; Frezzotti et al., 2002), and it is clear that more reliable accumulation data are needed.

There are many attempts to use remote sensing to estimate the surface mass balance based on the surface elevation changes (e.g. Wingham et al., 2006) or radar backscatter (Scambos et al., 2008; Rotschky et al., 2006). Rotschky et al. (2006) showed that there exists a relationship between SMB and SAR backscatter. They reported different regression coefficients for each of their scatterometer derived snow pack classes. They found the highest correlations (r=0.88, after elevation trend correction) for dry firn, low accumulation sites, which represents the largest part of the EAP. In this area we can neglect any dielectric losses due to the presence of water or scattering features resulting from refreezing processes. Thus, scattering by layering and snow grains is the dominating source of scattering losses in the firn pack. Low accumulation leads

to thinner layering and allows for the growth of larger snow grains (Courville et al., 2007), both are factors that lead to strong microwave backscatter and an inverse correlation between SMB and SAR backscatter (Forster et al., 1999; Rott et al., 1993). The relationship is sensitive to the regional characteristics, such as mean annual air temperature, and the relationship should always be calibrated for individual regions.

We present SMB estimates from GPR calibrated by firn cores taken during the traverse in Paper I. DEP and chemistry analysis of the cores allowed dating of firn layers by identifying several known volcanic events. We derived a mean SMB rate of 23.7±4.7 kg m^{-2} a^{-1} over the last 200 years from an 860 km long C-band GPR profile. In this study we establish an empirical relationship between the GPR derived SMB and SAR backscatter to estimate large scale variations of SMB. We derive a mean SMB rate of 26.3±3.3 kg m^{-2} a^{-1} over a 76000 km^2 large test area close to the ice divide. It can be further applied to the dry firn zone on the East Antarctic Plateau covered by SAR images. Comparisons to large scale mass balance studies in Antarctica show that our accumulation rates over the 200-year period lie in the lower range of the given 50-year period values, and indicate either a recent increase in accumulation rate or an overestimation of accumulation at the ice divide of up to 50% by the previous studies.

5.2 Study site

Our 860 km long profile goes across one of the least known parts of East Antarctica (Fig. 5.1). It is located along one of the main ice divides. Elevation increases from 3580 m to 3680 m southwards. The study area extents from 75.7° to 81.4° South and 20.1° to 44.7° East.

The annual mean temperature is about -50 °C (Comiso, 2000), and the annual mean wind speed remains usually below 6 m s^{-1} (Van Lipzig et al., 2004) in the study area. Previously, there have been very few direct measurements of SMB in this region (Anschütz et al., 2009; Picciotto et al., 1971). Analysis of five firn cores (NUS07-2, -3, -4, -5, and -6) along the profile indicate SMB less than 22 kg m^{-2} a^{-1} over the last 200 years (Anschütz et al., 2009).

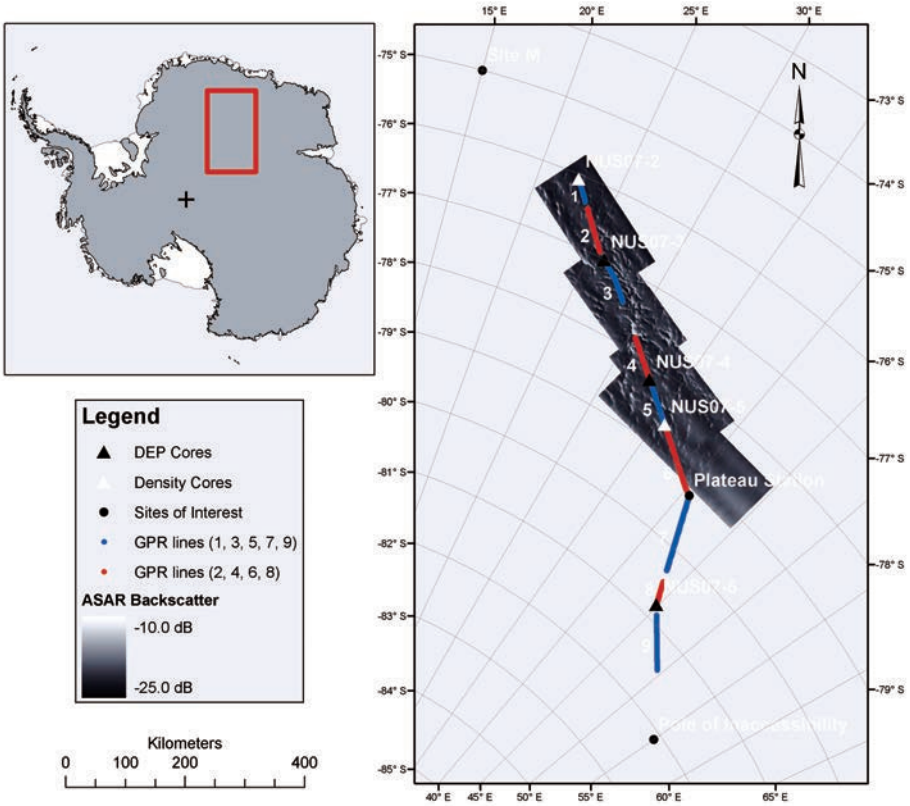

Fig. 5.1: *Location of the SAR images, GPR profiles and firn cores used in this study.*

5.3 Synthetic aperture radar

SAR scenes were taken by the C-band advanced synthetic aperture radar (ASAR) on-board the EnviSat satellite, launched by the European Space Agency (ESA) in 2002. Images were taken between November 2007 and January 2008, all in ascending pass. The largest temporal offset between ASAR and GPR records is 34 days. The polarization of the SAR images is HH and the swath number is IS2, corresponding to a near-range incident angle of 19.7° and a far-range incident angle of 26.8°. We applied radiometric correction to the single-look complex (SLC) images and corrected for the incidents angle variation over range. We reduced the range and azimuth resolution to reduce speckle from 7.0 m and 4.334 m, respectively, to 200 m in both directions. Images were orthorectified and a mosaic created from all images. From the mosaic, we extracted incident angle corrected backscatter values (γ^0) along the GPR profile. EnviSat can only operate up to 80° South, therefore no images were available south of Plateau Station (-79.25° N, 40.56° E) (Fig. 5.1).

5.4 SMB extended by ASAR backscatter

The Tambora layer identified in the firn cores was followed over the 860 km long GPR profile shown in Fig. 5.1. We presented SMB values between 9.1 and 38.2 kg m^{-2} a^{-1} along the profile with a mean SMB of 23.8±4.8 kg m^{-2} a^{-1} over the period from 1816 to 2007/2008 (Paper I).

In order to directly compare the γ^0 and SMB values at a specific location the SMB profile is averaged to the 200 m interval of the ASAR images using univariate spline interpolation. The linear regression between γ^0 and SMB is defined as

$$SMB = a \cdot \gamma^0 + b. \tag{5.4.1}$$

Table 5.1 summarizes the coefficients a, and b in equation 5.4.1 calculated for GPR sections 1 to 6 individually and for their sum. Profiles 1 to 5 have correlation coefficients (r) between -0.89 and -0.94 (Fig. 5.3). Profile 6 gives a low r of -0.32. Reasons for the low correlation are most likely due to the smooth profiles, both in SMB and γ^0. The mean SMB along profile 6 is 22.6 kg m^{-2} a^{-1} with a standard deviation of 1 kg

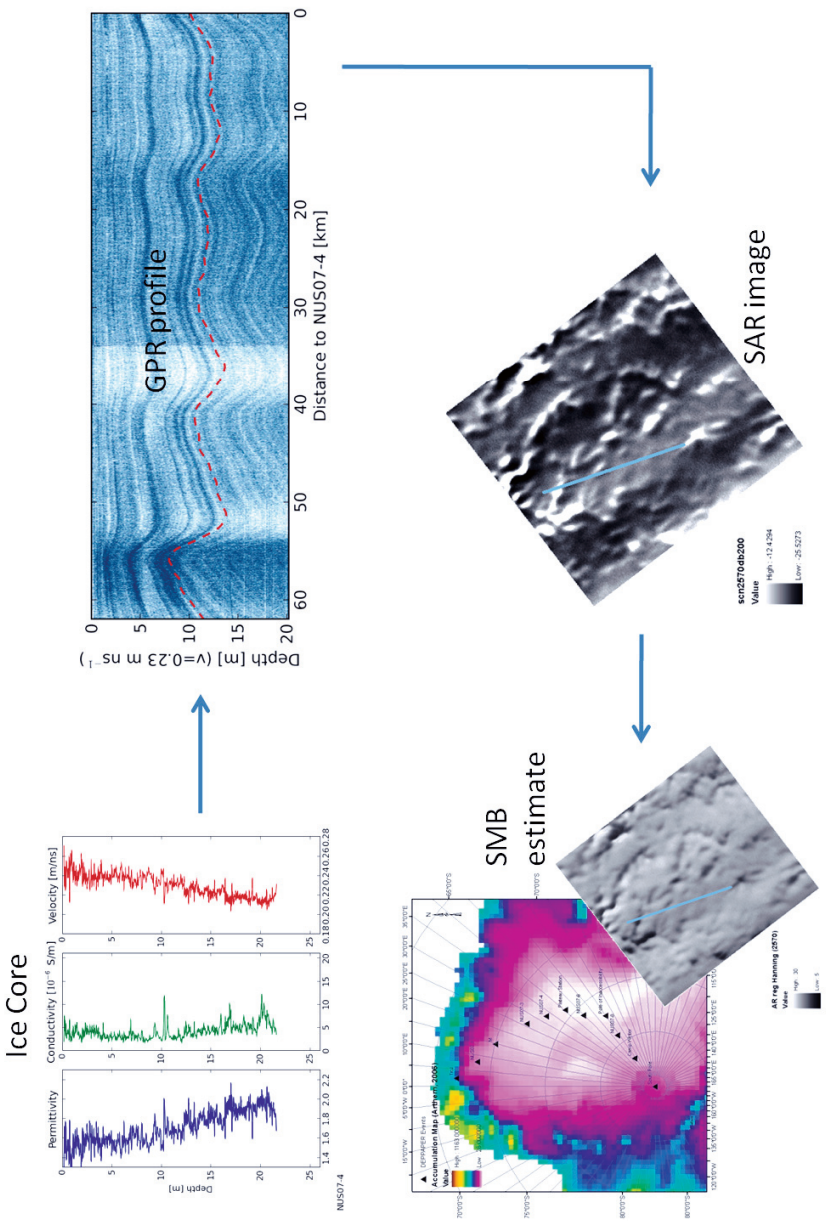

Fig. 5.2: *Ice cores give detailed insight in the accumulation history at a specific site. GPR is used to extend the SMB information from a point along a profile to determine SMB variability. Correlation between GPR derived SMB and SAR backscatter gives an SMB estimate over the spatial extent of the SAR scene.*

Table 5.1: *Regression and correlation coefficients for the regression between SMB and ASAR backscatter for GPR sections marked in Fig. 5.1.*

Profile	a	b	r^2
1	-3.23	-38.88	-0.94
2	-2.63	-22.14	-0.89
3	-2.60	-24.77	-0.93
4	-2.90	-31.24	-0.89
5	-2.25	-24.31	-0.90
6	-0.41	+14.42	-0.32
1-6	-2.11	-16.43	-0.66

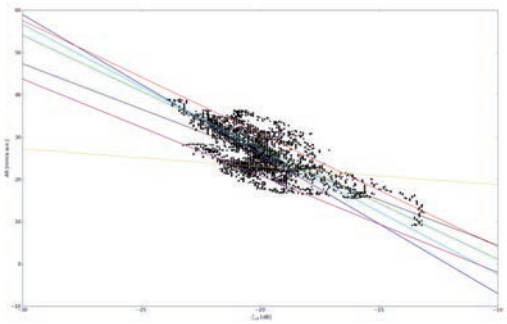

Fig. 5.3: *Cross-plot of GPR derived SMB versus EnviSat SAR backscatter along the profile. Except for one outlier the slopes are fairly constant.*

m^{-2} a^{-1}. γ^0 varies only by ± 1 dB in this section, which is close to the radiometric resolution of EnviSat's ASAR instrument.

These relations can be used to estimate the SMB over larger areas of the dry firn zone of the EAP, where SAR images are available. Applying equation 5.4.1 with the regression coefficients from profiles 1-6 from Table 5.1 to the ASAR mosaic (Fig. 5.1) gives a mean SMB of 26.2±3.3 kg m^{-2} a^{-1} for the 76000 km^2 large area. The minimum and maximum SMB over this area are 7.9kg m^{-2} a^{-1} and 38.1 kg m^{-2} a^{-1}, respectively. Fig. 5.2 illustrates the workflow.

The effective number of looks (ENL) has an impact on the correlation between SMB and γ^0. Reducing speckle noise flattens the backscatter spectrum along the profile. We

Table 5.2: *Mean snow accumulation rate along the profile.*

Reference	AR [kg m^{-2} a^{-1}]
This study	23.8 ± 4.8
Arthern et al. (2006)	35.1 ± 4.5
Monaghan et al. (2006)	27.9 ± 6.2
Van De Berg et al. (2006)	40.2 ± 2.5

used an ENL of 24 in range and 40 in azimuth, which gave a satisfying reduction of speckle while conserving the variations due to different firn properties.

5.5 Comparison to recent large-scale studies

In order to set our findings in relation to research done previously in this area we compared our results with three continent wide studies by Arthern et al. (2006), Monaghan et al. (2006) and Van De Berg et al. (2006). Fig. 5.4 shows the SMB variability obtained by GPR, using our empirical backscatter relationship (Eq. 5.4.1), and SMB previously estimated for the same area by other studies.

Monaghan et al. (2006) derived a 50 year time series of snowfall accumulation over Antarctica by combining ERA-40 precipitation models calibrated by in-situ measurements, mainly ice cores. They conclude that there has been no statistically significant change in snowfall accumulation over Antarctica in the period 1955-2004. Interestingly, the method by Monaghan et al. (2006) matches the level and the trend of our GPR derived SMB almost perfectly despite the fact that their results are also calculated only for the last 50 years.

Our results show that the 200-year mean SMB in this region is significantly lower than estimated for the last 50 years by Van De Berg et al. (2006) and Arthern et al. (2006) (Table 5.2, Fig. 5.4 and Fig. 5.5). The method of Arthern et al. (2006) describes the regional trend very well but their regional mean SMB is about 30% higher than our values.

Previous firn and ice core studies indicate that the SMB has increased at both ends of our GPR profile (Hofstede et al., 2004; Mosley-Thompson et al., 1999), and in several other places on EAP during the last 50 years (Frezzotti and Others, 2005; Oerter et al.,

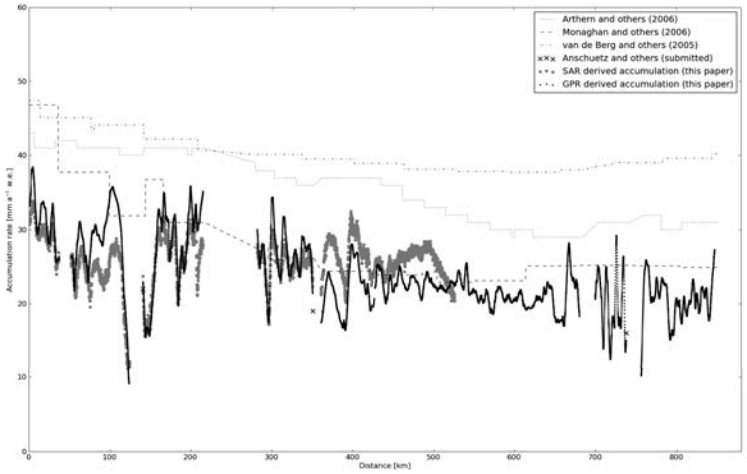

Fig. 5.4: *Our SMB rates from Paper I, SAR estimates and estimates by Arthern et al. (2006); Monaghan et al. (2006); Van De Berg et al. (2006) along the GPR profiles from Paper I.*

1999; Stenni and Others, 2002). Our area is located in the low wind speed region of EAP (Parish and Bromwich, 1991; Van Lipzig et al., 2004) where increasing ablation associated with increasing wind speeds due to climate change are not of importance, and a positive change in surface mass balance can be expected (Frezzotti and Others, 2004). However, it is not possible to evaluate with our data set if there is a recent change in accumulation rate.

5.6 Conclusions

Over areas where variations in SMB give rise to deflections in SAR backscatter above the radiometric resolution, a strong inverse correlation between the two exists. We used this correlation to extend the SMB derived by in-situ measurements (Anschütz et al., 2009) and GPR (Paper I). We applied this method over an area of 76000 km^2 and yielded a mean SMB of 26.2±3.3 kg m^{-2} a^{-1}. Advanced speckle filters, e.g. Frost or Gamma-Map filters, could improve correlation by preserving finer details, and thus helping to identify areas with low SMB variability or areas of zero or negative SMB.

Fig. 5.5: *Difference map between SMB derived by our SAR regression and continent wide SMB maps compiled by (Arthern et al., 2006; Monaghan et al., 2006; Van De Berg et al., 2006). We averaged our SMB vlaues from the pixels covered by a pixel from the large scale studies.*

Comparison of our study with SMB studies over the last 50 years (Arthern et al., 2006; Van De Berg et al., 2006) indicates that there has been a significant increase in SMB in the latter period of the last 200 years. The results show that the SMB point measurements by Anschütz et al. (2009) where located on the low accumulation sites along the profile giving up to 33% smaller SMB values than the profile mean.

5.7 Acknowledgments

Thanks to R. Storvold (Norut IT) for providing the SAR images and K. Casey (UiO) for creating the mosaic.

References

Anschütz, H., Müller, K., Isaksson, E., McConnell, J. R., Fischer, H., Miller, H., Albert, M. R., and Winther, J.-G. (2009). Revisiting sites of the South Pole Queen Maud Land Traverses in East Antarctica: Accumulation data from shallow firn cores. *J. Geophys. Res.*, 114(D24):D24106—-.

Arthern, R. J., Winebrenner, D. P., and Vaughan, D. G. (2006). Antarctic snow accumulation mapped using polarization of 4.3-cm wavelength microwave emission. *Journal of Geophysical Research*, 111, D0610.

Comiso, J. C. (2000). Variability and trends in Antarctic surface temperatures from in situ and satellite infrared measurements. *Journal of Climate*, 13:1674–1696.

Courville, Z. R., Albert, M. R., Fahnestock, M. A., Cathles, L. M., and Shuman, C. A. (2007). Impacts of an accumulation hiatus on the physical properties of firn at a low-accumulation polar site. *Journal of Geophysical Research*, 112(F2).

Forster, R. R., Jezek, K. C., Bolzan, J., and Gogineni, S. P. (1999). Relationships between radar backscatter and accumulation rates on the Greenland ice sheet. *International Journal of Remote Sensing*, 20:3131–3147(17).

Frezzotti, M., Gandolfi, S., La Marca, F., and Urbini, S. (2002). Snow dunes and glazed surfaces in Antarctica: new field and remote-sensing data. *Annals of Glaciology*, 34:81–88(8).

Frezzotti, M. and Others, . (2004). New estimations of precipitation and surface sublimation in East Antarctica from snow accumulation measurements. *Climate Dynamics*.

Frezzotti, M. and Others, . (2005). Spatial and temporal variability of snow accumulation in East Antarctica from traverse data. *Journal of Glaciology*, 51:113–124.

Hofstede, C. M., van de Wal, R. S. W., Kaspers, K. A., van den Broeke, M. R., Karlöf, L., Winther, J. G., Isaksson, E., Lappegard, G., Mulvaney, R., Oerter, H., and Wilhelms, F. (2004). Firn accumulation records for the past 1000 years on the basis of dielectric profiling of six firn cores from Dronning Maud Land, Antarctica. *Journal of Glaciology*, 50(169):279291.

Monaghan, A. J., Bromwich, D. H., Fogt, R. L., Goodwin, I., and Dixon, D. A. (2006). Insignificant Change in Antarctic Snowfall Since the Internatioanl Geophysical Year. *Science*, 313(827).

Mosley-Thompson, E., Paskievitch, J., Gow, M., and Thompson, L. (1999). Late 20th century increase in South Pole snow accumulation. *Journal of Geophysical Research*, 104(D4):38773886.

Oerter, H., Graf, W., Wilhelms, F., Minikin, A., and Miller, H. (1999). Accumulation studies on Amundsenisen, Dronning Maud Land, by means of tritium, dielectric profiling and stable-isotope measurements: first results from the 199596 and 199697 field seasons. *Annals of Glaciology*, 29:1–9.

Parish, T. R. and Bromwich, D. H. (1991). Continental-scale simulation of the Antarctic katabatic wind regime. *Journal of Climate*, 4(2):135146.

Picciotto, E., Grozaz, G., and de Breuck, W. (1971). Accumulation on the South Pole Queen Maud Land Traverse, 1964-1968. Antarctic Snow and Ice Studies II. *Antarc. Res. Ser.*, 16:257–315.

Rotschky, G., Rack, W., Dierking, W., and Oerter, H. (2006). Retrieving snowpack properties and accumulation estimates from a combination of SAR and scatterometer measurements. *IEEE Transactions on Geoscience and Remote Sensing*, 44(4):943–956.

Rott, H., Sturm, K., and Miller, H. (1993). Active and passive microwave signatures of Antarctic firn by means of field measurements and satellite data. *Annals of Glaciology*, 17:337–343.

Scambos, T., Haran, T., Frezotti, M., Jezek, K., Long, D., and K., F. (2008). Mapping East Antarctic wind glaze extent at high resolution from space: implications for East Antarctic ice mass balance. *Geophysical Research Abstracts*, 10, EGU200:SRef–ID: 1607–7962/gra/EGU2008–A–10755, EGU Genera.

Stenni, B. and Others, . (2002). Eight centuries of volcanic signal and climate change at Talos Dome (East Antarctica). *Journal of Geophysical Research*, 107(D9), 4.

Van De Berg, W. J., den Broeke, M. R., Reijmer, C. H., and Van Meijgaard, E. (2006). Reassessment of the Antarctic surface mass balance using calibrated output of a regional atmospheric climate model. *Journal of Geophysical Research*, 111(D11104).

Van Lipzig, N. P. M., Turner, J., Colwell, S. R., and den Broeke, M. R. (2004). The near-surface wind field over the Antarctic continent. *International Journal of Climatology*, 24:1973–1982.

Vaughan, D. G., Bamber, J. L., Giovinetto, M., Russell, J., and Cooper, A. P. R. (1999). Reassessment of net surface mass balance in Antarctica. *Journal of climate*, 12(4):933.

Wingham, D. J., Shepherd, A. P., Muir, A. S., and Marshall, G. J. (2006). Mass balance of the Antarctic Ice Sheet. *Phil. Trans. Roy. Soc. A.*, 364(1844):1627–1635.

Chapter 6

Paper II

Phase-center of L-band radar in polar snow and ice

Karsten Müller, Svein-Erik Hamran, Anna Sinisalo, and Jon-Ove Hagen

IEEE Transactions on Geoscience and Remote Sensing, in press.

Abstract

Backscatter from an aggregate of inhomogeneities combine to form an apparent surface reflection particularly in relation to interferometric synthetic aperture radar. The depth z_ϕ of this reflection can reside well below the true surface when the transmissivity at the interface between air and the aggregate is high. Snow and ice provide good examples, for which we calculate z_ϕ with different accumulation history and physical properties using a 0.5-3.0 GHz GPR. We acquired our data along transects in Antarctica and Svalbard. We find values of z_ϕ ¿ 40 m in low absorbing Antarctic firn and ≈10 meters in glaciers and ice shelves where melt-freeze cycles and lateral mass movement lead to an electrically more heterogeneous snow and ice column. The heterogeneity reduces dielectric contrast more rapidly with depth. Thus z_ϕ is found at shallower depth, but still resides several meters beneath the snow surface.

6.1 Introduction

Radar returns from a medium include scattering from its surface, scattering from internal inhomogeneities, and from the interface to the underlying medium. The strength of surface scattering is proportional to the relative complex dielectric constant of the surface (Ulaby et al., 1982), and its angular scattering pattern is governed by the surface roughness. The volume scattering strength is proportional to the dielectric contrasts between embedded inhomogeneities and that of the medium matrix and their density. Volumetric angular scattering pattern is determined by the roughness of the boundary surface, the average dielectric constant of the medium, and the geometric size of the inhomogeneities relative to the incident wavelength (Ulaby et al., 1982).

Reflections from media are actual composites of surface and volumetric backscatter. Only when the interface to the medium is flat and the medium is electrically homogeneous, does backscatter combine to produce an apparent surface reflection that aligns with the true surface. For electrically inhomogeneous media, especially when layered, the apparent surface reflection may occur well below the true surface.

The power penetration depth (z_P) is often used when evaluating the potential performance of a ground penetrating radar (GPR) for subsurface imaging. The depth z_P in a medium is where the power (P) of the electromagnetic field equals $P = P(0+)e^{-1}$, where $P(0+)$ is the power of the field after transmission into the medium and e is the base of the natural logarithm. z_P is a measure of how far an electromagnetic wave can travel inside the medium and depends on the total loss rate, which is the sum of the scattering and absorption (relaxation and conduction) losses. Absorption loss describes the transformation into other forms of energy, e.g. heat. Loss due to scattering means energy lost to directions other than that of incident radiation.

The *phase center* (z_ϕ) is the distance to an apparent surface reflection from a target. z_ϕ from an interface between two electrically homogeneous volumes is the distance between the receiver and the interface (Fig. 6.1a). If scatterers are distributed within the second volume z_ϕ extends inside the volume (Fig. 6.1b). The radar cross section of each scatterer and distribution of the scatterers inside the volume determine z_ϕ (Fig. 6.1c).

In elevation measurements using air- or space-borne radar, such as radar altimetry or InSAR, the penetration into the medium can bias the measurements (Dall et al.,

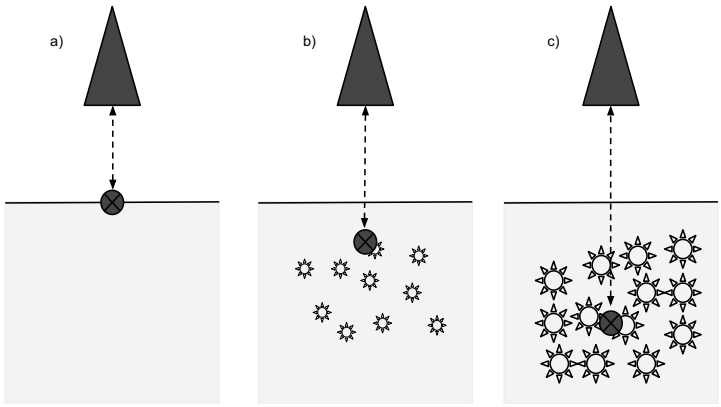

Fig. 6.1: *Phase center for various targets. The cross in the circle indicates the position of z_ϕ.* ***a)*** *For a flat interface between two electrically homogeneous volumes, z_ϕ aligns with the interface.* ***b)*** *and* ***c)*** *Dielectric inhomogeneities in the lower volume will pull z_ϕ inside the lower volume depending on the scatterer's radar cross section and distribution.*

2001). This bias is defined as the difference between the measured elevation and the true surface elevation (Dall, 2007). The bias is equal to z_ϕ of the volume scatterer measured by a nadir looking radar and independent of z_P. In case of an oblique incident wave at angle θ, which always occurs in InSAR measurements, the elevation bias will be

$$z_\phi \cos\theta. \tag{6.1.1}$$

Dry snow is highly transmissive at microwaves in the lower GHz region. At the air-snow interface only 2% of the incident energy are reflected, while the remaining 98% tranmit in the snow (Ulaby et al., 1982). Scatterers in snow are individual layers in the lower GHz region (Rott et al., 1993), while single snow grains act as scatterers at frequencies above 20 GHz (Hallikainen et al., 1986).

Direct measurements of z_ϕ, as the difference between laser and InSAR digital elevation models, gave 14 m at C-band (Dall et al., 2001) in dry polar firn and up to 120 m at L-band over glaciers in northeast Greenland (Rignot et al., 2001).

The objective of our paper is to show that the apparent surface reflection from snow lies at several meters depth below the actual snow surface. We calculate z_ϕ at L-band along GPR profiles in East Antarctica and on a glacier on Svalbard to show how z_ϕ varies in snow and ice with different accumulation history and physical properties.

Table 6.1: *Specifics of the gated ultra-wide band (UWB) radar. Firn* in the table has a relative permittivity of 1.8, corresponding to a density of 400 kg m^{-3} (Kovacs et al., 1995).*

Operation mode	Gated-FMCW
Center frequency	1.75 GHz
Bandwidth	2.5 GHz
Frequency steps	10^4
Frequency increment	250 kHz
Unambiguous range air/firn*	598/445 m
Nominal vertical resolution air/firn*	6/4.5 cm

The direct measurement by GPR ensures the inclusion of all scattering and absorption processes involved (in contrast to models).

6.2 Equipment and methodology

6.2.1 GPR system

We used the ultra-wide-band (UWB) radar described in (Ø yan et al., 2010) in gated frequency-modulated continuous-wave (FM-CW) mode for all measurements described in section 6.2.4. The system specifics are summarized in Table 6.1, where values given for firn relate to firn with a density of 400 kg m^{-3}.

The Vivaldi antennas (Plettemeier et al., 2009) of the GPR were separated by 0.1 m and are treated as monostatic. We suspended them 0.85 m above the snow surface extending from the side of a Berco TL6 tracked vehicle for the measurements in Antarctica. We collected traces every 0.1 s, which corresponds to a trace interval of approximately 0.2 m at an average driving speed of 2 m s^{-1}.

For the measurements on Svalbard we mounted the system on a sledge with an antenna height of 0.4 m above the ground and collected traces every 0.2 s, corresponding to a trace interval of approximately 0.4 m at an average driving speed of 2 ms^{-1}.

We gated the UWB radar by switching the transmitter and receiver on and off in an alternating scheme (Hamran et al., 1995; Ø yan et al., 2010). The recorded signal is therefore a convolution of the transmitter- and receiver-gating signals. Using

the same frequency and zero delay on both transmitter and receiver gates results in a window filter with maximum attenuation at time zero, maximum signal strength at the period of the gating frequency, and, again, maximum attenuation for signals arriving at times twice the gating period. We used a gating frequency of 1.0 MHz for the measurements in Antarctica and a gating frequency of 1.523123 MHz for the measurements on Svalbard.

6.2.2 Data processing

The radar records data in the frequency domain. We averaged the Antarctic data over 20 traces and the Svalbard data over 10 traces to improve the signal-to-noise ration (SNR). This corresponds to a distance interval of 4 m at a driving speed of 2 m s^{-1}. We applied a Hanning window filter and zero-padded each averaged frequency signal before we transferred it to time domain by inverse Fast Fourier transform (IFFT). Each trace contains 16384 samples with a time increment of 0.122 ns. We applied a static correction at 11 ns (sample 91) removing the direct wave. Time zero resides slightly above the snow surface reflection. We set the effective time window to 770 ns for Antarctic data and to 500 ns for Svalbard data, corresponding to ranges of 88.5 m and 57.5 m, respectively, assuming an electromagnetic velocity (c_{med}) of 0.23 m ns^{-1}.

We removed the influence of the gating gain by multiplying its inverse with the recorded traces and corrected the signal for geometrical spreading. The application of the gain is important so that our signal resembles the signal measured by a plane wave incident on the snow surface as from a space-borne radar.

We converted two-way travel time (t) to depth (d) by $d = 0.5 c_{med} t$. For the depth-conversion for all Antarctic profiles we used $c_{med} = 0.23$ m ns^{-1} ((Müller et al., 2010; Anschütz et al., 2009)). Medium velocities for the three profiles on Svalbard are averages of previously defined velocity-depth profiles (Langley et al., 2007) of 0.2 m ns^{-1} for the glacier ice zone and 0.23 m ns^{-1} in the superimposed ice (SI) and firn zone.

6.2.3 Estimating z_ϕ

Our radar measures backscatter amplitude at different frequencies $f_0 + N \cdot \Delta f$, where N is an integer between 0 and the maximum number of frequency steps Δf. Denoting

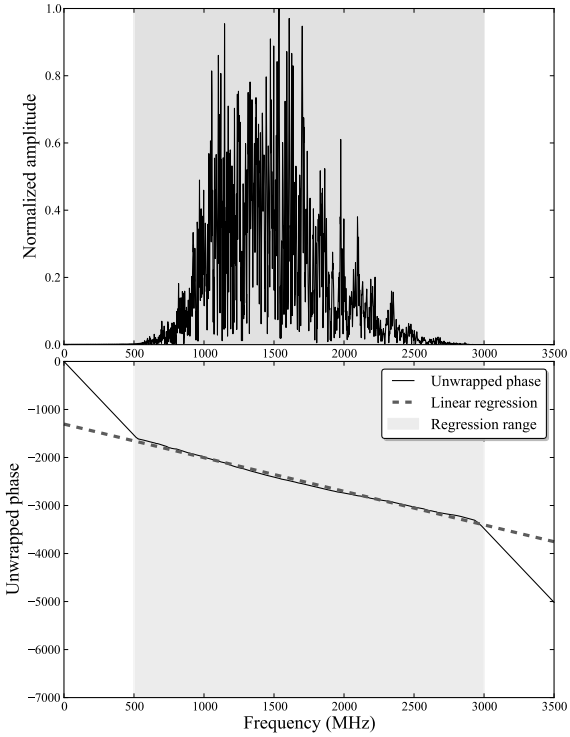

Fig. 6.2: *Calculation of the phase center. A linear regression is fitted to the unwrapped phase over the frequency range 0.5-3.0 GHz. The slope of the regression line multiplied by* $-c_0/(4\pi)$ *is the phase center.*

the phase difference between two backscatter measurements by $\Delta\phi$, then

$$\Delta\phi = 2\Delta k z_\phi = 4\pi\Delta f z_\phi c_{med}^{-1} \quad , \tag{6.2.1}$$

where $k = 2\pi f c_{med}^{-1}$ is the wavenumber and z_ϕ the distance to the target scattering phase center (Sarabandi, 1997). The phase center of the GPR signal is therefore

$$z_\phi = \frac{\Delta\phi}{2\Delta k} = \frac{\Delta\phi c_{med}}{4\pi\Delta f}, \tag{6.2.2}$$

where the factor 2 is due to the two-way travel path.

We calculate z_ϕ for each GPR trace by the following procedure. First we take the Fourier transform of the time domain signal yielding the amplitude and phase spectrum. The phase spectrum is then unwrapped. The slope of the unwrapped phase spectrum is now measured over the frequency range 0.5-3.0 GHz (Fig. 6.2) and multiplied by $-c_{med}/(4\pi)$ (equation 6.2.1).

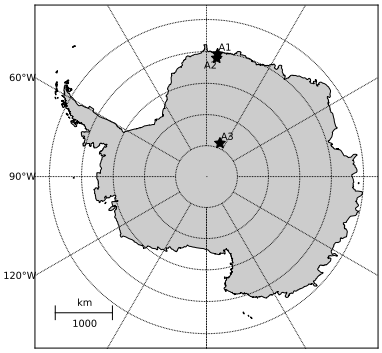

Fig. 6.3: *Map of Antarctica. The location of the profiles A1-A3 are marked by black stars.*

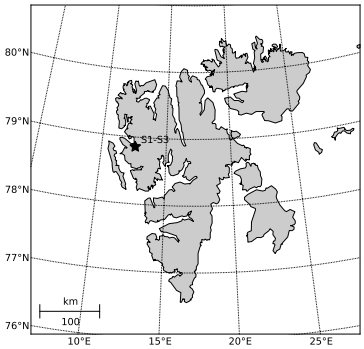

Fig. 6.4: *Map of Svalbard. The location of Kongsvegen glacier with the profiles S1-S3 is indicated by a black star.*

For an accurate calculation, it is important that the backscattered energy decays to the noise level within the applied time-window. If the length of the time-window is too short, energy from below is not considered in the calculation and the resulting z_ϕ will be too shallow.

6.2.4 Study sites

We calculated z_ϕ at six different sites in Antarctica and Svalbard (Fig. 6.3 and 6.4). These sites represent areas of different accumulation history, stratigraphy and physical properties of snow and ice (Table 6.2).

We collected all Antarctic profiles during the Norwegian - U.S. IPY traverse 2008/2009 (Goldman, 2008). Each is about 7 km long. Profiles A1 and A2 are from Fimbul ice shelf and in the near-coastal region of Dronning Maud Land (DML), respectively (Fig.

Table 6.2: *Location of the GPR profiles A1-S3 and mean phase center z_ϕ and its variability expressed by the standard deviation.*

Profile	Latitude	Longitude	Elevation	General Description	z_ϕ
A1	70.34°S	5.23°E	55 m	Fimbul ice shelf	9.6±0.8 m
A2	70.90°S	5.00°E	540 m	Coastal DML	17.5±2.9 m
A3	84.17°S	22.03°E	2640 m	Recovery Lakes	35-46 m
S1	78.80°N	12.96°E	420 m	Kongesvegen, ablation zone	10.1±1.7 m
S2	78.78°N	13.16°E	570 m	Kongesvegen, superimposed ice zone	12.4±1.8 m
S3	78.76°N	13.34°E	700 m	Kongesvegen, firn zone	10.1±0.7 m

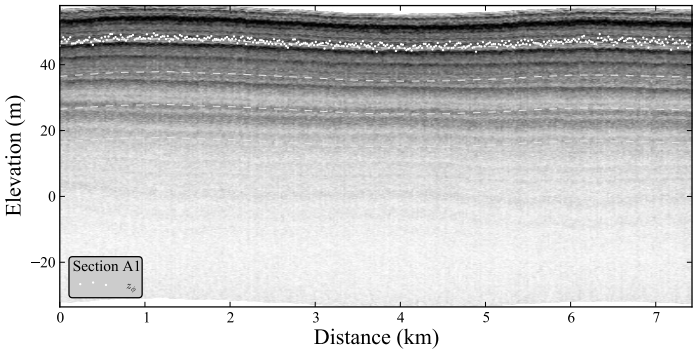

Fig. 6.5: *GPR profile A1 from the Fimbul ice shelf, Antarctica. White dashed lines indicate 10 m depth intervals. White dots indicate z_ϕ. The firn shows several strong reflection horizons. Two horizons at 3 m and 11 m appear strongest. z_ϕ aligns mostly with the 10 m depth contour exhibiting little lateral variations.*

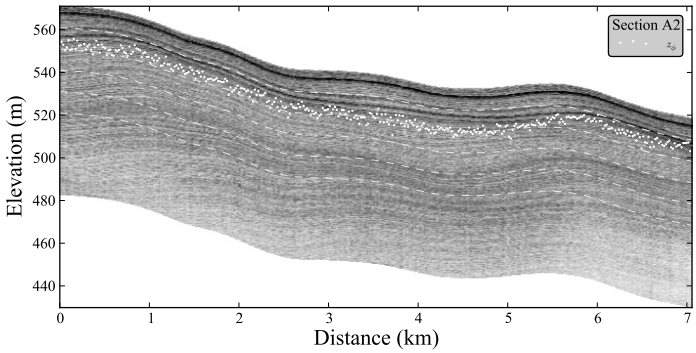

Fig. 6.6: *GPR profile A2 from coastal Dronning Maud Land, Antarctica. White dashed lines indicate 10 m depth intervals. White dots indicate z_ϕ. Undulations in the surface topography reflect in the firn stratigraphy. Two strong reflectors appear at around 4 m and 10 m depth. z_ϕ decreases from 5.5 km onwards aligning with a thinning of the firn layers.*

6.5 and 6.6). The annual surface mass balance (SMB) is on the order 30 kg m^{-2} a^{-1} and several melt events occur annually (Kaczmarska et al., 2006). The firn-ice transition is at 50-70 m depth (Kaczmarska et al., 2006).

Profile A3 (Fig. 6.7) is from the Recovery Lakes on the East Antarctica plateau (EAP). Annual SMB is on the order of 35 kg m^{-2} a^{-1} and lower (Anschütz et al., 2009; Arthern et al., 2006). Antarctic firn is composed of depth hoar layers alternating with fine-grained, high-density wind slabs (Alley, 1988). Depth hoar is low-density firn

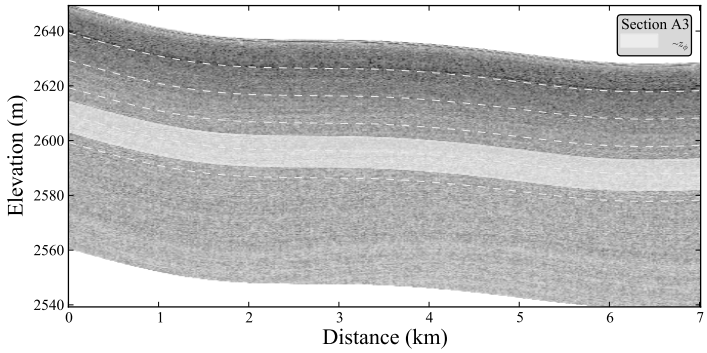

Fig. 6.7: *GPR profile A3 from the Recovery Lakes, Antarctica. White dashed lines indicate 10 m depth intervals. The white band indicates the potential position of z_ϕ. Scattering is very uniform with depth.*

or snow containing large, faceted, often cup-shaped crystals. It only exist if crystal growth is rapid, which requires large temperature gradients (>10 C m^{-1} (Colbeck, 1982)). Differences in the dielectric properties over depth in Antarctic firn are often related to depth hoar (Arcone et al., 2004). Firn thickness is on the order of hundred meters on the EAP. Thus, firn densification at A3 is slower over depth than at A1 and A2 (van der Veen et al., 1999).

Profiles S1-S3 are from the Arctic glacier Kongsvegen, which is situated close to the international research station Ny-Ålesund, Svalbard (Fig. 6.4). All three profiles are approximately 2.5 km long and were acquired in April 2008. All sites were dry at the time of data acquisition.

Profile S1 (Fig. 6.8) is in the ablation zone of the glacier where glacier ice is covered by 1-2 m winter snow at the time of the measurements (Hagen et al., 1999).

Profile S2 (Fig. 6.9) is from the superimposed ice (SI) zone. When surface melting occurs and melt-water can percolate some distance into the snow before it refreezes, ice lenses or glands can form within the snow or firn. When sufficient melt-water is produced the ice lenses and glands will form a continuous mass of ice. The zone where these ice masses are not buried beneath firn is called superimposed-ice (Paterson, 1994). GPR measurements compared to ice cores in the SI of Kongsvegen revealed that reflection horizons result from density contrasts caused by varying air bubble content in the ice layers (Langley et al., 2009).

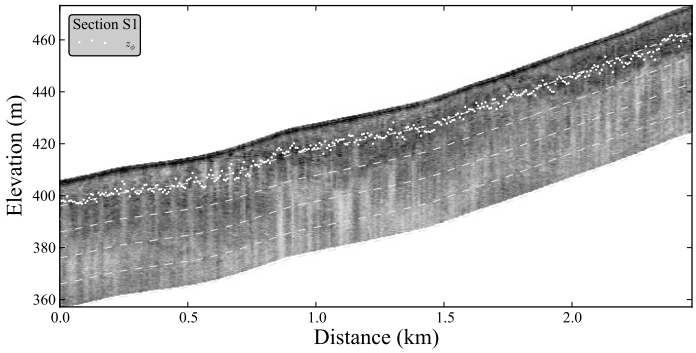

Fig. 6.8: *GPR profile S1 from the ablation zone of Kongsvegen, Svalbard. White dashed lines indicate 10 m depth intervals. White dots indicate z_ϕ. Patches of higher backscatter within the glacier ice are probably related to varying air bubble content. Lateral variations in z_ϕ are related to variations in backscatter by these patches.*

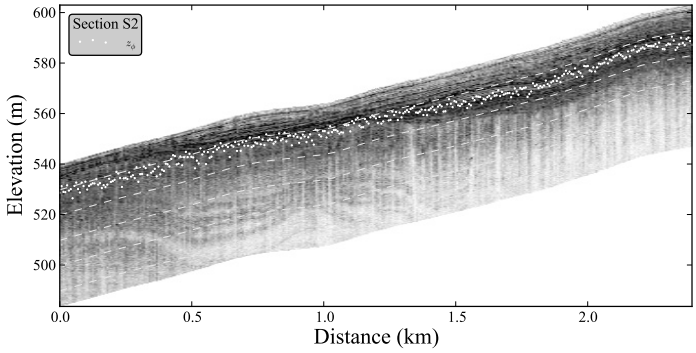

Fig. 6.9: *GPR profile S2 from the SI zone of Kongsvegen, Svalbard. White dashed lines indicate 10 m depth intervals. White dots indicate z_ϕ. The SI layers act as strong radar reflectors. With the increase in SI thickness at 1.3 km increases z_ϕ on average by 2 m.*

Profile S3 (Fig. 6.10) covers part of the firn zone of Kongsvegen. Here, thicker layers of firn are alternating with ice layers, that are thinner and less continuous, than in the SI (Hamran et al., 2009). Ice lenses of varying thickness from a few mm to >0.5 m within the firn have been identified in cores (Langley et al., 2009). The firn-ice transition is at 20-25 m depth (Hamran et al., 2009).

Melting or rain events can occur year-round on Svalbard and alter the composition of the snow and firn, resulting in a variable density distribution, both lateral and vertical (Langley et al., 2009).

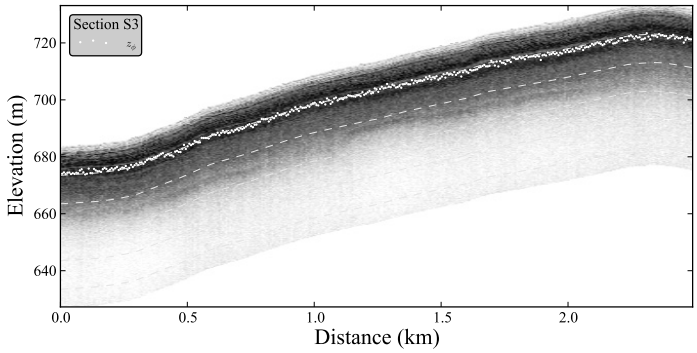

Fig. 6.10: *GPR profile S3 from the firn zone of Kongsvegen, Svalbard. White dashed lines indicate 10 m depth intervals. White dots indicate z_ϕ. The dominating scatterers are found in the top 5-15 m. The firn-ice transition is marked by a broad diffuse horizon at around 25 m depth. z_ϕ aligns with the 10 m depth contour exhibiting little lateral variations.*

6.3 Results

Mean values of z_ϕ from our GPR profiles are summarized in Table 6.2. The GPR profiles A1-S3 with calculated values for z_ϕ for each trace are shown in Fig. 6.5-6.10.

6.3.1 Antarctic profiles

Profile A1 is dominated by two strong horizons near 4 m and 11 m depth, that enclose z_ϕ along the profile (Fig. 6.5). Two, slightly weaker horizons appear near 15 m and 22 m depth. Backscatter from below 35 m depth is very weak.

Profile A2 has an undulating surface topography (Fig. 6.6). The GPR profile shows several strong reflection horizons, especially in the top 20 m. Distances between the strong horizons become shorter towards the right side of the profile due to decreasing snow accumulation, which corresponds to steeper slopes (Arcone et al., 2005). z_ϕ lies below the strong horizon at 10 to 12 m depth and follows its shape.

Profile A3 on the Antarctic plateau shows fine layered firn without significant lateral or vertical variations (Fig. 6.7). The scattering appears very uniform throughout the profile. We could not calculate z_ϕ for profile A3 with our method, because the energy was not attenuated to the noise level within our time-window. Thus, energy returning from scatterers below the time-window would pull z_ϕ down. We test if the true phase

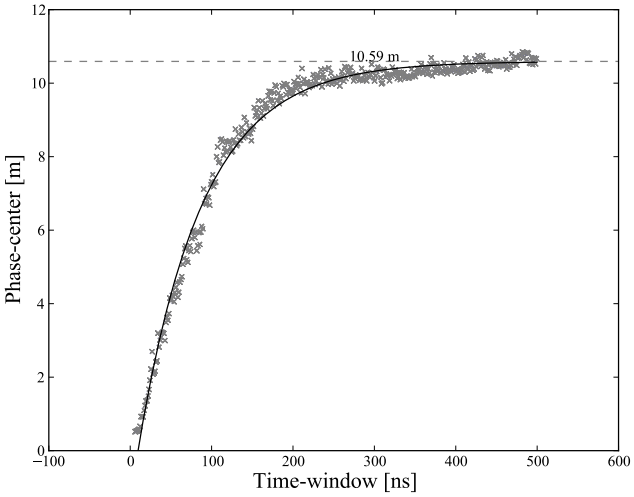

Fig. 6.11: *Example from profile S3, where z_ϕ lies well within the time-window. The value of z_ϕ fluctuates around the true phase center after the time-window extends beyond 300 ns. The fluctuation occurs, because random noise is added with further extension of the time-window. This z_ϕ vs. time-window curve characteristic is found for traces in all profiles apart from A3. Fitting the function $f = -ae^{-bx} + c$ to the values, puts the asymptote at 10.59 m.*

center lies within our time-window by extending the time-window from a few ns to its maximum and calculating z_ϕ for each time-window. If the true value lies within the maximum time-window the curve is asymptotic (Fig. 6.11). From a certain point on the z_ϕ vs. time-window curve fluctuates around the true phase-center. That fluctuation is determined by noise. If the values are outside the time-window the curve shows a positive gradient over all time-windows (Fig. 6.12). We estimated the potential z_ϕ in A3 to be about 35-46 m by applying the above analysis (Fig. 6.7).

6.3.2 Svalbard profiles

The GPR data from Kongsvegen are described in (Hamran et al., 2009). Profile S1 (Fig. 6.8) shows high backscatter from the upper 2 m, probably related to the previous-summer-surface (PSS) separating winter snow and glacier ice (Langley et al., 2009). The underlying glacier ice shows patches of high backscatter (Hamran et al., 2009). One patch extends laterally from 0-0.8 km and vertically from 10-30 m. The second

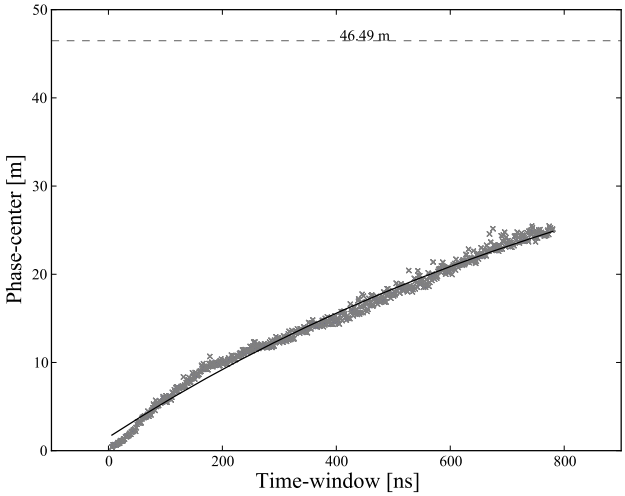

Fig. 6.12: *Example trace from A3, where z_ϕ is still influenced by backscattered energy from below our time-window. z_ϕ is approximately linear increasing for an increasing time-window, indicating the noise level is not reached at the end of the trace. The asymptote of the fitted asymptotic function $f = -ae^{-bx} + c$ lies at 46.5 m (dashed gray line) and might indicate the true phase-center.*

patch is found in the upper 20 m extending laterally from 0.8-2.5 km. The patches of increased backscatter are probably related to variations of the amount and size of enclosed air bubbles in the glacier ice (Hamran et al., 2009). z_ϕ is about 10 m along the entire profile.

The PSS is found at 1-2 m depth below the winter snow over profile S2 (Fig. 6.9). Beneath the PSS, the thickness of the SI ranges from 5 m at 0.0 km to 25 m at 1.8 km. z_ϕ lies below or aligns with the bottom of the SI over the first half of the profile until 1.3 km. In the second half, with considerably thicker SI, z_ϕ is on average 2 m deeper and embedded between strong backscatter from the bottom of the SI and a strong reflection horizon within the SI near 10 m depth.

A continuous, broad band of high backscatter extending from 4-20 m depth is visible along the entire profile S3 (Fig. 6.10). The transition between firn and ice is likely to cause the diffuse reflection horizon near 25 m depth. No significant lateral variations are visible. z_ϕ follows the center of the band, dropping from 8 m depth at the start of

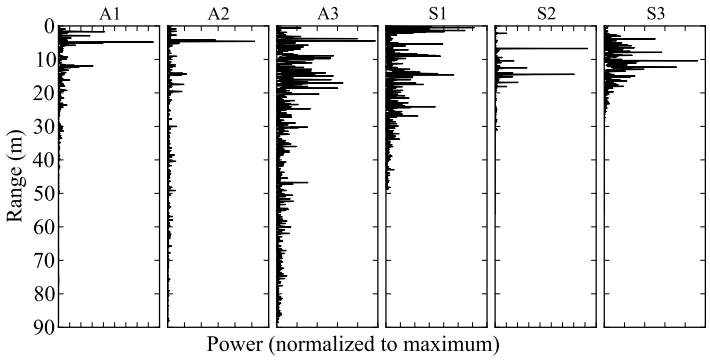

Fig. 6.13: *Example traces from the center of profiles A1-S3. The power is normalized to the maximum value in each trace. Profiles A1, A2 and S2 show distinct reflections. Profiles A3 and S1 have a more uniform scattering over depth. Profile S3 has a cluster of reflection horizons at 5-15 m.*

the profile to 10 m at the end. z_ϕ is well defined. The GPR trace S3 in Fig. 6.13 shows that most energy is returned from 5-15 m depth. The absence of lateral variations in the stratigraphy is also represented by the low standard deviations of 0.7 m from mean z_ϕ.

Our values of z_ϕ use the static correction as the reference plane. This introduces a bias in z_ϕ with regard to the true snow surface of 15 cm for Svalbard measurements and 60 cm for measurements in Antarctica.

6.4 Discussion

We observe an increase in z_ϕ between profile A1 at the exterior of Antarctica and profile A3 on the EAP (Table 6.2), as has been reported by (Davis and Poznyak, 1993). In Antarctic firn, z_ϕ is greater where the firn-ice transition is deeper. This is due to preserved density contrasts at greater depths between ice layers or wind-slaps and surrounding firn. Thus, more energy is scattered back from greater depth. If firn density increases faster with depth, the dielectric contrasts between firn and embedded ice layers become significantly smaller with depth and the relative amount of energy backscattered from deeper parts has less influence on z_ϕ. For example, firn density (ρ) at 40 m depth on Fimbul ice shelf is $\approx$800 kg m^{-3} (Kaczmarska et al., 2006), whereas it

is ≈600 kg m^{-3} at the same depth at South Pole (van der Veen et al., 1999). Converting these densities to the respective refractive index n by $n = 1 + 0.851\rho$ (Kovacs et al., 1995) and calculating the Fresnel reflection coefficient (R) for each with respect to ice ($\rho_i = 916$ kg m^{-3}) we see that R from a firn-ice interface on the ice shelf at 40 m depth is an order of magnitude lower than R from a firn-ice interface at South Pole.

Our mean z_ϕ of 17.5±2.9 m at profile A2 is slightly deeper than the 14±4 m reported from Greenland summit as the difference between a laser altimeter and the air-borne TOPSAR (Rignot et al., 2001). When we correct the mean offset of 14 m by the nominal look-angle of TOPSAR of 45° (Zebker et al., 1992) using (6.1.1), we yield z_ϕ =19.8 m, suggesting that z_ϕ in continental Greenland and coastal Antarctica (A2) are very similar, as is the depth to the firn-ice transition of 70 m (Zwally and Jun, 2002; Schwander et al., 1997).

Our estimate of z_ϕ of 35-46 m at A3 indicates that there exists a substantial bias for radar elevation measurements over large parts of the EAP.

Our z_ϕ values on Kongsvegen vary around 10 m (S1-S3 in Table 6.2) comparable to those from A1 on the ice shelf. z_ϕ along S1 is determined by two features. The first are reflections related to the PSS and the second are patches of high backscatter in the glacier ice. Lateral variations in z_ϕ are due to lateral variations in the backscatter strength from the patches, since the PSS related scattering is fairly constant.

The SI gives the highest radar backscatter within the time-window in profile S2 (Fig. 6.9). Firn is the source of the strongest backscatter along profile S3 (Fig. 6.10). The SI and firn in S2 and S3 show distinctively stronger backscatter than snow above or ice below (see traces in Fig. 6.13). The firn thickness is rather constant explaining the stable position of z_ϕ along S3. Increasing thickness of the SI in S2 leads to a deeper z_ϕ, indicating that the transition from SI to glacier ice has large influence on z_ϕ.

Scattering along S1-S3 is neither uniform over depth nor lateral as in A3. Despite these variations in backscatter we measure a similar z_ϕ along the three profiles S1-S3. The lateral variation in z_ϕ decreases with elevation.

Our z_ϕ estimates for the Svalbard glacier between 10-12 m agree with the ∼13±7.6 m (after angle correction) reported for Brady and Reid glacier, Alaska at L-band (Rignot et al., 2001). Thus indicating, that z_ϕ is on the order of 10-15 m for maritime glaciers, such as Kongsvegen, Brady and Reid glacier. Our similar values of z_ϕ in dif-

ferent parts of the glacier support the findings that z_ϕ is independent of the glacier zone (Rignot et al., 2001).

Major differences in z_ϕ exist between the profiles A1-S3. Values range from 5.6 m to more than 46 m. The standard deviations from the mean z_ϕ along each profile range from 0.7-2.9 m. The variation is therewith equal or larger than the SMB at the sites. Thus, time-lapse InSAR with frequencies in the lower GHz region are not suitable for detecting changes in SMB. Changes in z_ϕ between two InSAR measurements might be due to different viewing geometries or a different seasonal state of the snow obscuring changes due to a change in SMB.

6.5 Conclusions

We showed that the phase-center (z_ϕ) of a plane wave incident on snow or ice lies well below the snow surface. In Antarctic firn, where scattering is uniform over depth, the depth to the firn-ice transition and therewith the rate of densification influences z_ϕ. A deeper firn-ice transition corresponds to deeper z_ϕ.

If backscatter is relatively high over a certain part of the investigated time-window, z_ϕ is pulled towards the high backscatter part. Localized high backscatter in snow can result from melt-layers (A1), SI with varying air bubble content (S2) or alternating firn and ice layers (S3) embedded in electrically more homogeneous snow or ice.

In snow with a few defined reflection horizons (A1, S3) z_ϕ is most stable. Local variations in z_ϕ are equal to or larger than the SMB and might obscure changes in elevation attributed to changes in SMB by time-lapse InSAR at low GHz frequencies.

In order to determine the actual position of z_ϕ on the EAP the time-window of our GPR needs to be increased. The position of z_ϕ can be influenced by system noise when signals are weak. Good knowledge of the system noise and the capability to effectively remove it in the data is necessary for more accurate measurements, especially over weak scattering targets like glacier ice with a small number of impurities.

Acknowledgment

This work has been carried out under the umbrella of TASTE-IDEA (Trans-Antarctic Scientific Traverses Expeditions – Ice Divide of East Antarctica) within the frame-

work of IPY project 152 funded by Norwegian Polar Institute, the Research Council of Norway, and the National Science Foundation of the United States and the IPY GLACIODYN project funded by the Research Council of Norway. This work is also a contribution to ITASE (International Trans-Antarctic Scientific Expedition). Mats-Jørgen Øyan is gratefully acknowledged for carrying out the GPR survey on Svalbard. Special thanks goes to the Norwegian-U.S. traverse team 2008/2009. The authors very much appreciate the thoughtful and constructive review by Steve Arcone and an anonymous reviewer, which certainly improved the paper.

References

Alley, R. B. (1988). Concerning the deposition and diagenesis of strata in polar firn. *Journal of Glaciology*, 34(118):283–290.

Anschütz, H., Müller, K., Isaksson, E., McConnell, J. R., Fischer, H., Miller, H., Albert, M. R., and Winther, J.-G. (2009). Revisiting sites of the South Pole Queen Maud Land Traverses in East Antarctica: Accumulation data from shallow firn cores. *J. Geophys. Res.*, 114(D24):D24106—-.

Arcone, S. A., Spikes, V. B., and Hamilton, G. S. (2005). Phase structure of radar stratigraphic horizons within Antarctic firn. *Annals of Glaciology*, 41:10–16.

Arcone, S. A., Spikes, V. B., Hamilton, G. S., and Mayewski, P. A. (2004). Stratigraphic continuity in 400 MHz short-pulse radar profiles of firn in West Antarctica. *Annals of Glaciology*, 39:195–200.

Arthern, R. J., Winebrenner, D. P., and Vaughan, D. G. (2006). Antarctic snow accumulation mapped using polarization of 4.3-cm wavelength microwave emission. *Journal of Geophysical Research*, 111, D0610.

Colbeck, S. C. (1982). An overview of seasonal snow metamorphism. *Rev. Geophys.*, 20(1):45–61.

Dall, J. (2007). InSAR elevation bias caused by penetration into uniform volumes. *Geoscience and Remote Sensing, IEEE Transactions on*, 45(7):2319–2324.

Dall, J., Madsen, S. N., Keller, K., and Forsberg, R. (2001). Topography and penetration of the Greenland Ice Sheet measured with airborne SAR Interferometry. *Geophys. Res. Lett.*, 28(9):1703–1706.

Davis, C. H. and Poznyak, V. I. (1993). The depth of penetration in Antarctic firn at 10 GHz. *Geoscience and Remote Sensing, IEEE Transactions on*, 31(5):1107–1111.

Goldman, H. V. (2008). From the editor: halfway through the IPY - halfway for an Antarctic traverse. *Polar Research*, 27:1–6.

Hagen, J.-O., Melvold, K., Eiken, T., Isaksson, E., and Lefauconnier, B. (1999). Mass balance methods on Kongsvegen, Svalbard. *Geogr. Ann.*, 81 A(4):593–601.

Hallikainen, M., Ulaby, F., and Abdelrazik, M. (1986). Dielectric properties of snow in the 3 to 37 GHz range. *IEEE Transactions on Antennas and Propagation*, 34(11):1329–1340.

Hamran, S. E., Gjessing, D. T., Hjelmstad, J., and Aarholt, E. (1995). Ground penetrating synthetic pulse radar: dynamic range and modes of operation. *Journal of Applied Geophysics*, 33(1-3):7–14.

Hamran, S. E., Ø yan, M. J., and Kohler, J. (2009). UWB radar profiling reveals glacier facies. In *Proceedings IWAGPR*.

Kaczmarska, M., Isaksson, E., Karlø f, L., Brandt, O., Winther, J. G., van de Wal, R. S. W., van den Broeke, M., and Johnsen, S. J. (2006). Ice core melt features in relation to {A}ntarctic coastal climate. *Antarctic Science*, 18(02):271–278.

Kovacs, A., Gow, A. J., and Morey, R. M. (1995). The in-situ dielectric constant of polar firn revisited. *Cold Regions Science and Technology*, 23(3):245–256.

Langley, K., Hamran, S.-E., Hø gda, K.-A., Storvold, R., Brandt, O., Hagen, J.-O., and Kohler, J. (2007). Use of C-Band Ground Penetrating Radar to Determine Backscatter Sources Within Glaciers. *Geoscience and Remote Sensing, IEEE Transactions on*, 45(5).

Langley, K. A., Lacroix, P., Hamran, S.-E., and Brandt, O. (2009). Sources of backscatter at 5.3 GHz from a superimposed ice and firn area revealed by multi-frequency GPR and cores. *Journal of Glaciology*, 55:373–383(11).

Müller, K., Sinisalo, A., Anschütz, H., Hamran, S. E., Hagen, J. O., McConnell, J. R., and Pasteris, D. R. (2010). An 860 km surface mass-balance profile on the {E}ast {A}ntarctic plateau derived by {GPR}. *Annals of Glaciology*, 51(55):1–8.

Ø yan, M. J., Hamran, S. E., Hanssen, L., Berger, T., and Plettemeier, D. (2010). Ultra Wideband Gated Step Frequency Ground Penetrating Radar. *Geoscience and Remote Sensing, IEEE Transactions on*, submitted.

Paterson, W. S. B. (1994). *The physics of glaciers*. Pergamon, 3rd edition.

Plettemeier, D., Ciarletti, V., Hamran, S.-E., Corbel, C., Cais, P., Benedix, W.-S., Wolf, K., Linke, S., and Roddecke, S. (2009). Full polarimetric GPR antenna system aboard the ExoMars rover. In *Radar Conference, 2009 IEEE*, pages 1–6.

Rignot, E., Echelmeyer, K., and Krabill, W. (2001). Penetration depth of interferometric synthetic-aperture radar signals in snow and ice. *Geophys. Res. Lett.*, 28(18):3501–3504.

Rott, H., Sturm, K., and Miller, H. (1993). Active and passive microwave signatures of Antarctic firn by means of field measurements and satellite data. *Annals of Glaciology*, 17:337–343.

Sarabandi, K. (1997). Delta-k-radar equivalent of interferometric SAR: a theoretical study for determination of vegetation height. *Geoscience and Remote Sensing, IEEE Transactions on*, 35(5):1267–1276.

Schwander, J., Sowers, T., Barnola, J.-M., Blunier, T., Fuchs, A., and Malaiz, B. (1997). Age scale of the air in the summit ice: Implication for glacial-interglacial temperature change. *J. Geophys. Res.*, 102(D16):19483–19493.

Ulaby, F. T., Moore, R. K., and Fung, A. K., editors (1982). *Microwave Remote Sensing: Active and Passive*, chapter Physical m. Addison-Wesley Publishing Company.

van der Veen, C. J., Mosley-Thompson, E., Gow, A. J., and Mark, B. G. (1999). Accumulation At South Pole: Comparison of two 900-year records. *J. Geophys. Res.*, 104(D24):31067–31076.

Zebker, H. A., Member, S., Madsen, S. N., Martin, J., Wheeler, K. B., Miller, T., Lou, Y., Alberti, G., Vetrella, S., and Cucci, A. (1992). The TOPSAR Interferometric Radar Topographic Mapping Instrument. *IEEE Transactions on Geoscience and Remote Sensing*, 30(5):933–940.

Zwally, H. J. and Jun, L. (2002). Seasonal and interannual variations of firn densification and ice-sheet surface elevation at the Greenland summit. *Journal of Glaciology*, 48:199–207(9).

Chapter 7

Paper III

Change in microwave scattering mechanisms along Kongsvegen glacier, Svalbard and implications for SAR monitoring.

Karsten Müller, Svein-Erik Hamran, Anna Sinisalo, and Jon-Ove Hagen

in prep.